The Paroxysmal Precipitation of the Desert: Flash Floods in the Southwestern US

James A. Smith[1],Mary Lynn Baeck[1],Long Yang[1],Julia Signell[1], Efrat Morin[2],David C. Goodrich[3]

[1]Department of Civil and Environmental Engineering, Princeton University, Engineering Quadrangle, Princeton, NJ 08540.
[2]Institute of Earth Sciences, Hebrew University, Jerusalem, Israel
[3]USDS-ARS, Tucson, Arizona, USA

Key Points:

- The 14 September 2015 Hildale Storm was a hailstorm that produced catastrophic flooding in southern Utah.
- The climatology of monsoon thunderstorms that produce flash floods in the Southwestern US exhibits large spatial heterogeneity.
- Record flood peaks in many Colorado Plateau watersheds over a wide range of basin scales are produced by small, monsoon thunderstorms that pass close to the basin outlet.

Corresponding author: James A Smith, `jsmith@princeton.edu`

Abstract

The 14 September 2015 Hildale, Utah storm resulted in 20 flash flood fatalities, making it the most deadly natural disaster in Utah history; it is the quintessential example of the "paroxysmal precipitation of the desert". The measured peak discharge from Maxwell Canyon at a drainage area of 5.3 km^2 was 266 $m^3\ s^{-1}$, a value that exceeds envelope curve peaks for Utah. Close analyses of the 14 September 2015 storm are at the center of this study; we compare structure, motion and evolution of the Hildale Storm with properties of a large sample of flash flood producing storms in southern Utah and northern Arizona and a smaller population of storms producing record and near-record floods in Colorado Plateau drainage basins. The 14 September 2015 flash flood reflects features common to other major flash flood events in the region, as well as unique features. The flood was produced by a hailstorm that was moving rapidly from southwest to northeast and intensified as it interacted with complex terrain. We characterize rainfall and thunderstorm variability over the Southwestern US study region using radar observations from flash flood producing storms and observations from the National Lightning Detection Network. The hydroclimatology of flash flooding, which we examine through analyses of USGS flood peak records, exhibits relatively weak dependence on drainage basin area. Large flood peaks over a broad range of basin scales can be produced by small thunderstorms like the 14 September 2015 Hildale Storm, which pass close to the basin outlet.

1 Introduction

"Sooner or later the cloudburst visits every tract, and when it comes the local drainage-way discharges in a few hours more water than is yielded to it by the ordinary precipitation of many years... So far as may be judged from the size of the channels draining small catchment basins, the rare, brief, paroxysmal precipitation of the desert is at least equal while it lasts to the rainfall of the fertile plain." G. K. Gilbert [1890]

Gilbert used the term paroxysmal in its dictionary formulation, "marked by bursts of destructive force or intense activity" (Merriam-Webster), to describe the storms that shape the channels of southwestern US rivers. Gilbert's insights were grounded in observations made during field investigations with the Surveys of the southwestern US (Powell (1895)), especially those leading to his landmark studies of the Henry Mountains (Gilbert (1877)) and Lake Bonneville (Gilbert (1890)). The broad objective of this study is motivated by Gilbert's apt description of southwestern US storms: we look to characterize the paroxysmal nature of precipitation for extreme flash-flood producing storms in the southwestern US.

The 14 September 2015 "cloudburst" in southern Utah resulted in 20 flash flood fatalities, making it the most deadly natural disaster in Utah history (Deseret News, 15 September 2015). It is the quintessential example of the storms Gilbert described. Of the 20 fatalities, 13 occurred in Hildale, Utah and resulted from flooding in Short Creek. The remaining 7 fatalities occurred 20 km to the north when hikers were trapped by floodwaters in a slot canyon in Zion National Park. The 20 fatalities were the product of a single hailstorm. Polarimetric radar observations show that the storm exhibited striking temporal variability, with the Maxwell Canyon tributary of Short Creek and a small portion of the East Fork Virgin River basin experiencing extreme precipitation. Close analyses of the 14 September 2015 storm are at the center of this study (Section 4); we will compare structure, motion and evolution of the Hildale Storm with properties of a large sample of flash flood producing storms in southern Utah and northern Arizona (Section 3) and a smaller population of storms producing record and near-record floods in Colorado Plateau drainage basins (Figure 1).

Peak discharge measurements made by the U. S. Geological Survey (USGS) for the 14 September 2015 flood in Short Creek at a drainage area of 58 km^2 and for the Maxwell Canyon tributary at a drainage area of 5.3 km^2 are both 266 $m^3\ s^{-1}$ (personal commu-

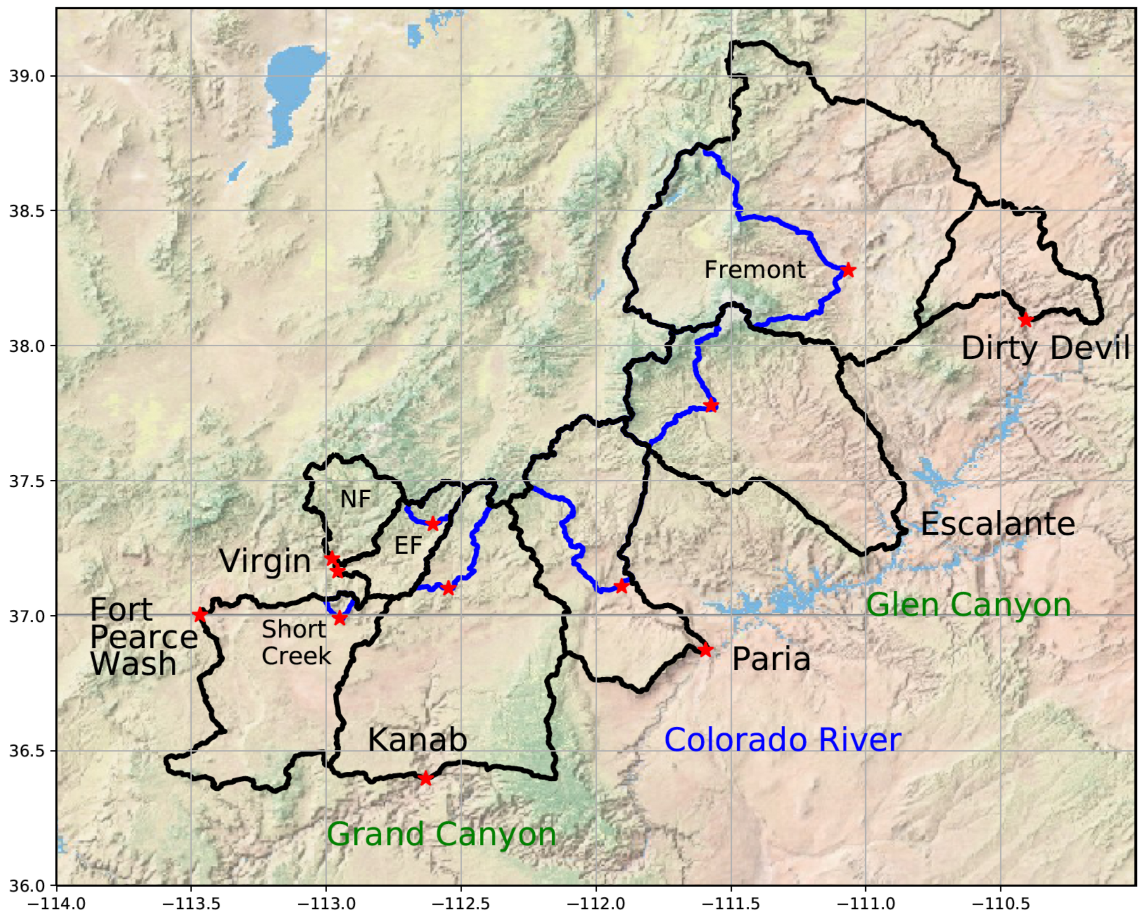

Figure 1. Basin boundaries for the Kanab Creek, Paria River, Escalante River, Dirty Devil River and Virgin Rivers basins (outer basins are outlined in black). Blue Boundaries are for gaged sub-basins. Short Creek, the setting of the 14 September 2015 flood, is a sub-basin of Fort Pearce Wash. Locations of stream gaging stations are denoted by red stars.

nication from Cory Angeroth on 27 June 2016). The 266 m^3 s^{-1} flood peak for Maxwell Canyon is on the envelope curve of flood peaks for the Colorado Plateau (Figure 2; see Enzel et al. (1993); see aslo Crippen and Bue (1977), Thomas et al. (1994), Berwick (1962), Thomas and Lindskov (1983) and Webb et al. (1988)). The dependence of flood peak magnitudes on drainage area is relatively weak in southwestern US rivers, compared to other regions of the US (Thomas and Lindskov (1983) and Thomas et al. (1994); see also Etheredge et al. (2004)). Flood peak magnitudes are closely linked to storm scale - cloudbursts, like the Hildale Storm, can produce record flood peaks over a wide range of drainage areas, as will be shown in Sections 4 and 5.

The Short Creek flood occurred 41 years to the day after the event that produced, by far, the most extreme flood peak measurement in the region (Figure 2) - the Eldorado Canyon flood of 14 September 1974 produced a peak discharge of 2150 m^3 s^{-1} at a drainage area of 50 km^2. Maximum flood peak measurements for basin scales up to 10,000 km^2 do not exceed the Eldorado Canyon peak. “Intense rainfall, thunder and hail” accompanied the Eldorado Canyon flood (Glancy and Harmsen (1975)).

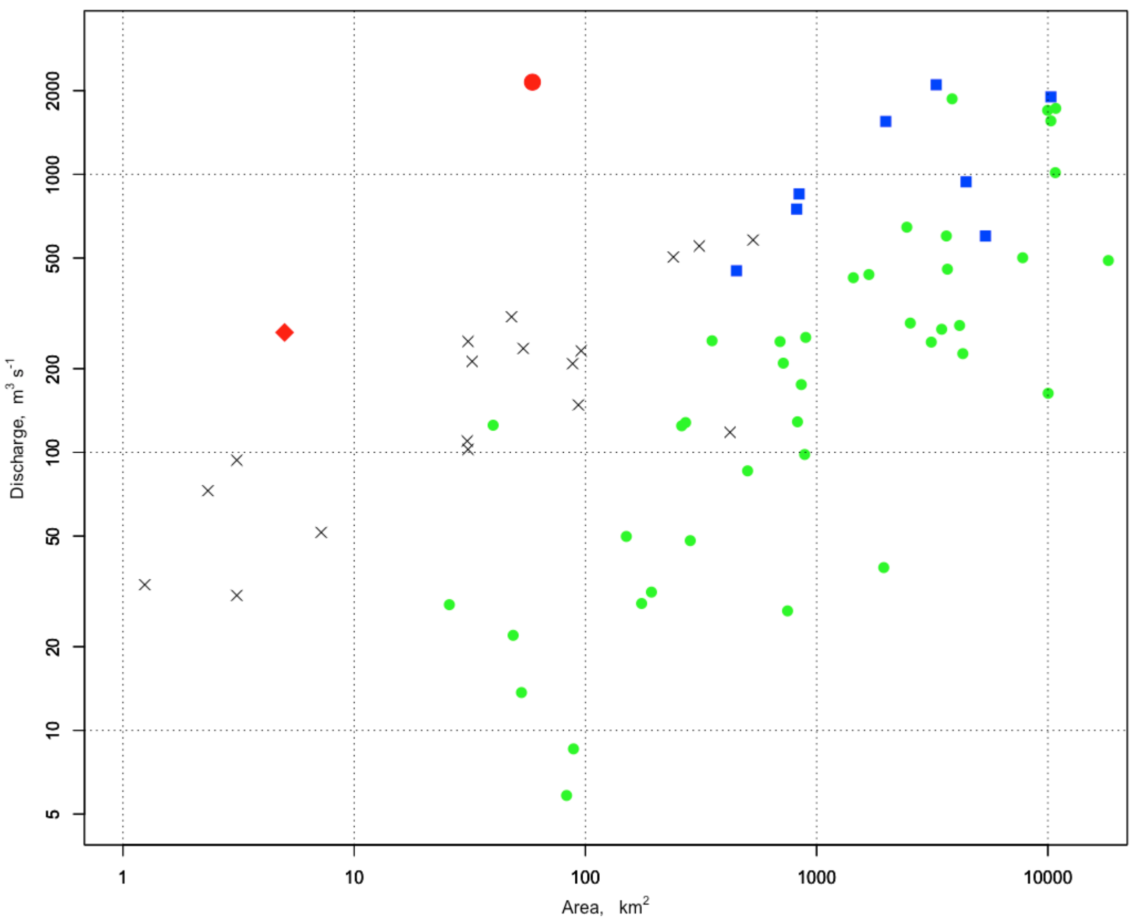

Figure 2. Record flood peaks in the southwestern US study region, with the 14 September 2015 peak from Maxwell Canyon shown as a red diamond. The green circles are record flood peaks from USGS stream gaging stations. Flood peaks denoted by black "x" are are from the "miscellaneous" record in Utah (Crippen and Bue (1977)). The flood peaks in blue are paleoflood peaks from (Enzel et al., 1993). The 14 September 1974 Eldorado Canyon flood peak is shown as a red circle.

Cloudburst storms have an extensive legacy as agents of flash flooding in the southwestern US (see, for example, Woolley (1946), Leopold (1942), Leopold (1946), Hales (1975), Webb et al. (1988) and Hjalimarsom and Thomas (1992)). These storms typically occur during the North American Monsoon (NAM) season, which peaks during July and August and extends into September (Adams and Comrie (1997), Maddox et al. (1980), Higgins et al. (1997), Watson, López, and Holle (1994), Vivoni et al. (2006), Luong et al. (2017), Mazon et al. (2016), Maddox et al. (1995), Hu and Dominguez (2015), Corbosiero et al. (2009), K. M. Wood and Ritchie (2013), Pascale et al. (2017) and Bieda et al. (2009)). The climatology of thunderstorms exhibits considerable variability over the North American Monsoon season and major flood events from organized systems of thunderstorms in the Colorado Plateau extend into October. The mixtures of storm structure and motion that produce record floods are closely linked to the seasonal cycle of thunderstorms.

In the southwestern US it is difficult to know when and where cloudbursts occur, even with modern observing capabilities. The study region includes some of the most remote areas of the conterminous US and the density of rain gages and stream gages is low. We rely heavily on polarimetric radar observations (see, for example, Kumjian and Ryzhkov (2008), Romine et al. (2008), Kumjian (2013), Ryzhkov et al. (2013) and Cunha et al. (2013)) to examine rainfall and storm properties. Specific differential phase shift measurements (Kumjian (2013)) play an especially important role in detection of exceptional rainfall rates. In many regions of the southwestern US, it is difficult to obtain useful radar measurements due to blockage problems associated with mountainous terrain (Maddox et al. (2003)). In southern Utah, the National Weather Service (NWS) avoided this problem by deployment of the Cedar City, Utah WSR-88D on the top of Blow Hard Mountain at an elevation of 3.2 km MSL (V. T. Wood et al. (2003)). This is fortuitous in allowing us to examine storm properties without the problems of terrain blockage. The elevation of the radar, however, means that we can not see what is of most interest, rainfall near the ground surface. The lowest beam of the Cedar City radar samples the atmosphere above Short Creek at an elevation of approximately 3 km above ground level.

Gilbert's observations on the "size of channels" in small southwestern US watersheds presaged the "arroyo problem", which centers on observations that channels in Colorado Plateau rivers incised and widened dramatically in the second half of the 19th century (see, for example, Graf (1983), Webb and Hereford (2001) and Harvey and Pederson (2011)). Most arroyos began to fill by the middle of the 20th century (Leopold (1976)). Explanations for the sequence of alterations to Colorado Plateau river channels center on the climatology of extreme rainfall (Leopold (1976), Graf (1983) and Webb et al. (1988)). Gilbert's observations point to a broader issue - channels in small southwestern US watersheds can be larger and deeper than their counterparts in the "fertile plain". Both the arroyo problem and the larger problems of drainage evolution in southwestern US rivers require advances in understanding the nature of extreme rainfall from thunderstorm systems during the North American Monsoon (Adams and Comrie (1997), Higgins et al. (1997), Morin et al. (2005), Watson, Holle, and Lopez (1994) and Vivoni et al. (2006); see Ely et al. (1994) and Ely (1997) for discussion of winter storms and flooding in the southwestern US).

The September 2015 Hildale, Utah storm was a severe thunderstorm which produced hail and copious lightning. The most intense hailstorms have been discounted as important flood agents. (Cotton et al., 2010) note that "storms producing the largest hailstones occur in strongly sheared environments; thus, in general, we should not expect that the storm systems producing the largest hailstones are also heavy rain producing storms." (Doswell et al., 1996), (Smith et al., 2001) and (Rogash & Racy, 2002) provided a different perspective, noting that the most intense hailstorms, supercell thunderstorms, are important flood hazards in the US (see also Hitchens and Brooks (2013), Nielsen et al. (2015), Smith et al. (2018) and Nielsen and Schumacher (2018)). Extensive research on hailstorms has provided a broad characterization of their structure and evolution (see, for example, Kumjian et al. (2015) and Hubbert et al. (1998)). An issue that has not been resolved is how heavy rainfall is distributed within a hailstorm and how the structure and evolution of extreme rainfall within a hailstorm is linked to storm dynamics and microphysics (see, for example, Romine et al. (2008) and Kumjian et al. (2015)). The occurrence of hail and extreme rainfall rates in close proximity is an important feature of some of the most extreme floods in the US (Smith et al. (2018)).

We compare structure and evolution of the 14 September 2015 storm with the larger population of thunderstorms that produce flash floods in the region. Climatological analyses of storm properties are based on a catalog of flash flood days during the period from 1998 - 2016 in southern Utah and northern Arizona. Flash flood reports in the National Center for Environmental Information (NCEI) Storm Events data set are used to select the flash flood days. We examine storm structure and evolution through Lagrangian analyses of storm motion, size and convective intensity, based on storm tracking of 3-D reflectivity fields using the TITAN algorithms (Dixon and Wiener (1993)). We use measures of convective intensity derived from storm tracking algorithms, including maximum reflectivity and echo top height in the tracked storm cell (Dixon and Wiener (1993), Tapia et al. (1998) and Javier et al. (2007)).

The climatologies of flash floods and thunderstorms in the southwestern US are linked. Thunderstorm climatology for the region is examined through analyses of Cloud-to-Ground (CG) lightning data from the National Lightning Detection Network (NLDN; see Reap and MacGorman (1989), Watson and López (1994),Watson, López, and Holle (1994), King and Balling Jr. (1994), Petersen and Rutledge (1998), Lang and Rutledge (2002), Deierling and Petersen (2008) and Villarini and Smith (2013)). Lightning climatology provides only a rough depiction of flash flood climatology in the southwestern US - virtually all of the flash floods during the NAM season are from thunderstorms, but only a small fraction of thunderstorms produce major flash floods.

The 14 September 2015 Hildale storm intensified rapidly as it approached the Short Creek watershed and the Vermillion Cliffs, which form the southwestern boundary of the watershed. Complex terrain plays a central role in determining the spatial and temporal structure of rainfall in the study region. The links between mountainous terrain and storm initiation are especially important elements of the climatology of thunderstorms and flash floods in the Colorado Plateau. Terrain can also enhance pre-existing convection, especially on windward slopes, and contribute to development and evolution of severe thunderstorms (Bosart et al. (2006)). The interplay of spatial heterogeneity of storm evolution and drainage network structure (Morin et al. (2006)) suggests that mountainous watersheds should exhibit distinctive patterns of flood response that will be unique to the specific settings in the landscape (see Smith et al. (2018) for discussion of this issue for other mountainous settings in the US). The interaction of storm structure and evolution with complex terrain introduces pronounced spatial heterogeneities into the flood hydroclimatology of the study region.

Questions that motivate the study include the following: 1) What are the characteristic patterns of storm structure and evolution for extreme flood producing storms in arid/semi-arid regions? 2) How does extreme flood response in arid/semi-arid watersheds depend on temporal and spatial variability of rainfall rate? 3) What are the storm and terrain features that control spatial heterogeneity of flood peaks? 4) What are the precipitation mechanisms associated with extreme rainfall rates? 5) Are all basins in the Colorado Plateau “unique” in their flood hazards?

2 Data and Methods

The climatology of thunderstorms in the southern Utah - northern Arizona study region is examined through analyses of cloud-to-ground (CG) lightning observations from the NLDN (see Orville (2008) and Cummins and Murphy (2009)). Our analyses are based on observations during the period 1991 - 2016 and we restrict consideration to negative strikes with intensities less than -10 kA (see Cummins et al. (1998) and Villarini and Smith (2013)).

We use polarimetric radar fields from the Cedar City WSR-88D radar to examine storm structure and motion and to assess spatial and temporal variability of rainfall rate; the polarimetric upgrade of the Cedar City radar occurred in 2012. We primarily examine two polarimetric radar fields: horizontal reflectivity (Z_H) and specific differential phase shift (K_{DP}); an introduction to radar polarimetric measurements can be found in (Kumjian, 2013). Horizontal reflectivity Z_H provides an aggregate characterization of number and sizes of hydrometeors. Differential reflectivity Z_{DR} is the ratio between the horizontal and vertical reflectivity and provides information on characteristic sizes of raindrops and hydrometeor type. Differential phase shift Φ_{DP} (in degrees) is the difference in phase shift between the horizontal and vertically polarized waves. Specific differential phase K_{DP} (degrees km^{-1}) is the range derivative of the differential phase shift along a radial radar beam. K_{DP} is dependent on the size as well as number concentration of rain drops, and provides a useful tool for detecting heavy rainfall.

We converted WSR-88D Archive Level-II fields from radial coordinates into 3-D Cartesian grids using the RADX tools developed at the NCAR Research Applications Lab. Specific differential phase (K_{DP}) is computed in polar space. All the fields (including horizontal reflectivity Z_H and differential reflectivity Z_{DR}) are gridded using a three dimensional linear interpolation scheme. Reflectivity and differential reflectivity are converted from dB to linear, gridded and then back to dB. The spatial resolution of the gridded radar fields is 1 km. The time required for the radar to complete a full volume scan of the atmosphere is 5-6 minutes. Volume scan observations for the 14 September 2015 storm include multiple base scans providing a time resolution of 2-3 minutes for low elevation measurements of polarimetric variables.

To examine storm structure, motion and size for flash flood producing storms we performed storm tracking analyses of 3-D reflectivity fields derived from KICX volume scan reflectivity data. Flash flood reports from the NCEI Storm Events data base provided the sample of storm events. Storm days consisted of all days (1200 UTC - 1200 UTC) with flash flood reports in the northern Arizona - southern Utah study region during the NAM period (July - September) for the years from 1998 - 2015. We omitted days for which WSR-88D reflectivity observations were not available, resulting in a total of 360 days.

Lagrangian analyses were based on the TITAN storm tracking algorithms (Dixon and Wiener (1993); see also Tapia et al. (1998), Javier et al. (2007) and Yang et al. (2017) for related analyses). A reflectivity threshold of 45 dBZ and volume threshold of 5 km^3 were used to identify convective storm elements (see Dixon and Wiener (1993)). We also restricted analyses to elevations above 3 km MSL to account for radar elevation. Variables computed from tracking analyses include location of the storm centroid, echo top height (45 dBZ), maximum reflectivity in the storm (dBZ), storm speed, storm direction and storm area. Analyses focus on intense storm elements, which we take to be tracked storm elements with echo tops greater than 8.5 km (above radar elevation); elevation of the KICX radar is approximately 3 km MSL.

We use operational polarimetric rainfall fields developed by the NWS from the KICX radar to examine rainfall rate variability over large watersheds. The digital polarimetric rainfall (DPR) rainfall fields are converted from polar coordinates to a regular 1 km grid using the NOAA Weather and Climate Toolkit. The DPR algorithm uses specific differential phase shift to estimate rainfall rate in hail and it uses reflectivity and differential reflectivity to estimate rainfall rate when the hydrometeor classification is rain. Using gridded DPR rainfall rate fields, we examine rainfall relative to the drainage network using the rainfall-weighted flow distance to the basin outlet (see Smith et al. (2002) and Smith et al. (2005)). Elevation of the radar beam limits the accuracy of rainfall rate fields, but they provide useful tools for examining the effects of rainfall location, relative to the basin outlet, on flood response.

We use USGS stream gaging records, and especially the annual maximum flood peak record (see Ryberg et al. (2017) for a recent description), to examine flood peak distributions. Measurements of many extreme floods are made by indirect discharge methods, involving field measurements of peak water surface profiles and channel cross-sections, combined with hydraulic computations (Costa and Jarrett (2008) and Koenig et al. (2016)). Indirect measurements are made for floods at stream gaging sites when the gage is destroyed or fails to operate properly. They are also made at miscellaneous sites, i.e. sites that do not have stream gaging stations, typically for the most extreme floods. The 14

September 2015 peak discharge measurements in Short Creek are in the miscellaneous site category. Peak discharge from indirect measurements have significant errors, especially for the most extreme flood peaks (see discussion and references in Smith et al. (2018)). Paleohydrologic reconstructions of flood peaks also play an important role in examining the upper tail of flood peaks in the southwestern US (as in Figure 2; see Webb et al. (1988), Enzel et al. (1993), Ely (1997) and Baker (2008)).

KINEROS-2 is a physically based rainfall runoff model developed for watersheds in semi-arid environments (Morin et al. (2006), Goodrich et al. (2011) and Schaffner et al. (2016)). The model represents the watershed as a cascade of overland flow planes and channels. In our KINEROS-2 model formulation for Maxwell Canyon at a drainage area of 5.3 km^2, we have 120 overland flow planes and 50 channel segments. The structure of the overland flow planes and channels conforms with field inspection by the authors in November 2016. We used the Automated Geospatial Assessment (AGWA) routines, developed by the USDA-ARS (Goodrich et al. (2011)) for implementing KINEROS-2.

Downscaling simulations with the Weather Research and Forecasting (WRF) model are used to examine the storm environment for the 14 September 2015 storm. WRF was implemented in three one-way nested domains with horizontal grid resolutions of 9, 3 and 1 km, respectively. The physics parameterizations used in this study include: (1) WSM6 for cloud microphysics; (2) YSU for planetary boundary layer (PBL); (3) Rapid Radiative Transfer Model (RRTM) and (4) Dudhia scheme for longwave and shortwave radiation, respectively. No cumulus parameterization is used. North American Regional Reanalysis (NARR) fields are used for initial and boundary conditions (for similar implementations, see Smith and Baeck (2015), Smith et al. (2018) and Yang et al. (2017)).

3 Study Region and Thunderstorm Climatology

Thunderstorms are the dominant agent of flash flooding in much of the Colorado Plateau and the climatology of thunderstorms provides insights to the climatology of flash flooding. In this section we examine the thunderstorm climatology in the southwestern US study region through analyses of cloud-to-ground (CG) lightning observations from the NLDN (see Orville (2008) and Cummins and Murphy (2009)). We use storm tracking analyses of 3-D reflectivity fields for 360 flash flood days to examine the climatology of storm structure, motion and convective instensity.

There are striking spatial heterogeneities in thunderstorm frequency over the study region and these features are strongly linked to terrain (Figure 3). The largest lightning flash densities are located in high elevation plateau regions of the Colorado Plateau and the mountains to the west in the Basin and Range province. The boundary between the Colorado Plateau and Basin and Range provinces is roughly the low elevation region extending northeast to southwest from the Escalante Desert through the Virgin River Valley to Lake Mead (Figure 3). The Basin and Range includes the northeast portion of the Mojave Desert. Mean annual CG flash densities vary by more than a factor of 5 from the high elevation regions of the Shivwits Plateau, Kaibab Plateau, Aquarius Plateau, Kaiparowits Plateau, Paunsaugunt Plateau, Markagunt Plateau and Pine Valley Mountains to low elevation regions including Lake Mead, the Virgin River Valley, the Escalante Desert and Glen Canyon (see Figure 3 for locations). Peak CG flash densities exceed 3 strikes km^{-2} over Boulder Mountain in the Aquarius Plateau (3450 meters MSL) and over Mount Dellenbaugh at the southwest end of the Shivwits Plateau (2130 meters MSL). Flash densities are less than 1.5 strikes km^{-2} in the Grand Canyon, just south of the Shivwits Plateau. Mean annual CG flash densities are less than 0.6 CG strikes km^{-2} over portions of Lake Mead, Glen Canyon and the Escalante Desert.

The changes in elevation moving south to north from the Grand Canyon into the Markagunt, Paunsaugunt and Kaiparowitz Plateaus are conceptualized in terms of a se-

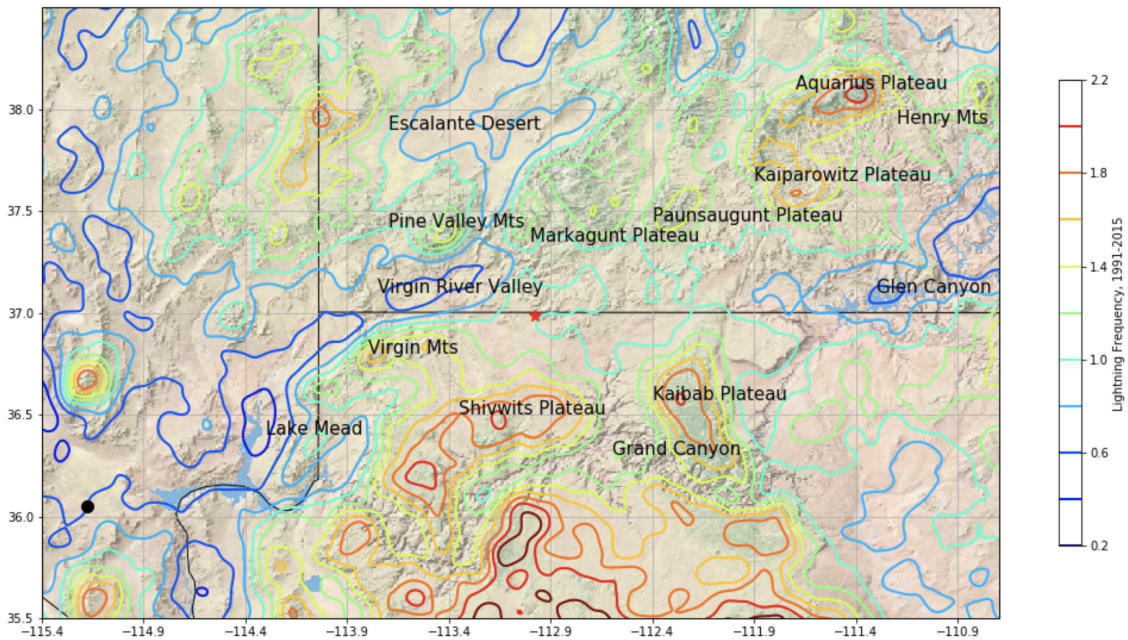

Figure 3. Mean CG flash density (strikes km^{-2}) for southern Utah, northern Arizona and eastern Nevada. Geographic features are labeled. The red star shows the location of the Short Creek stream gaging station. The Las Vegas radiosonde location is denoted by a black circle.

quence of discrete jumps in elevation, termed the Grand Staircase. The second step is the Vermillion Cliffs and it marks the boundary of the Short Creek drainage basin (Figure 3); as will be seen below, terrain boundaries are locations of large gradients in rainfall and lightning for the 14 September 2015 storm.

Virtually all of the thunderstorms in the study region occur during the July - September period that defines the NAM season (Figure 4). In the figure we show boxplots of the area with daily CG flash density exceeding 1 CG strike km^{-2} (top) and 2 CG strikes km^{-2} (bottom) for the period 1991 - 2006. The transition into the monsoon season is abrupt (Figure 4); the median area with flash density greater than 1 CG strike km^{-2} is close to 0 for June. The frequency of major thunderstorms outbreaks peaks during August, with a significant decline into September. Thunderstorm frequency in October is also small, but October thunderstorm systems are linked to extreme flood peaks in the study region, as will be shown in Section 5.

Individual thunderstorms that occur in the study region during the NAM season have spatial scales that are typically smaller than 50 km^2, as detailed below. During thunderstorm days, the total area affected by these storms is often several orders of magnitude larger than the scale of the individual storms. The median area with flash density exceeding 1 CG strike km^{-2} is 1600 km^2 in July, 2100 km^2 in August and less than 200 km^2 in September (Figure 4). The median area with CG flash density exceeding 2 CG strikes km^{-2} peaks at 480 km^2 in August. Structure and evolution of thunderstorms, relative to terrain, play a central role in determining the extremes of flood-producing rainfall, as detailed in Section 5.

The climatology of thunderstorms in the study region is coupled to the seasonality of water vapor (Figure 5). Boxplots of CG flash density, stratified by values of precipitable water at Page, Arizona, highlight the dependence of thunderstorm occurrence

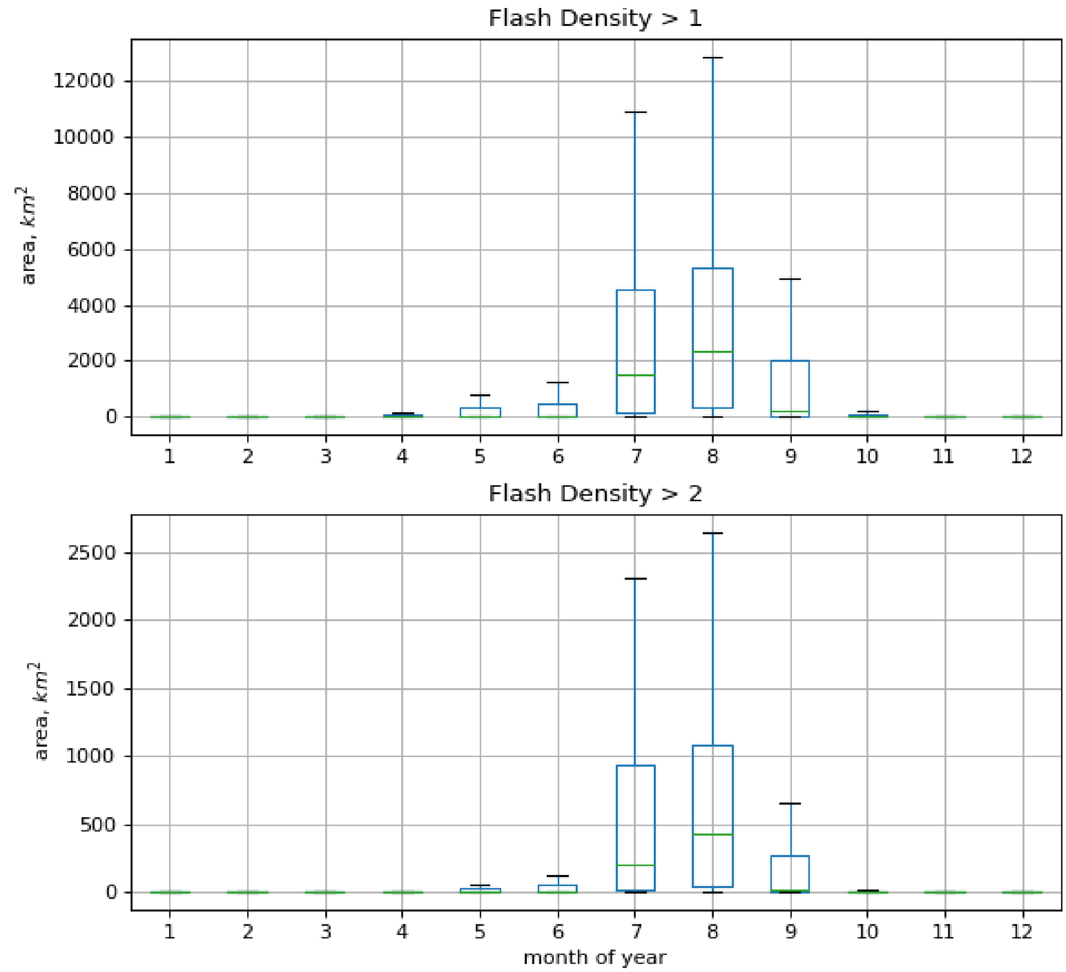

Figure 4. Monthly boxplots of daily area with CG flash density exceeding 1 km^{-2} (top) and 2 km^{-2} (bottom). Month 1 is January.

on water vapor. The increase in thunderstorm frequency during the North American Monsoon season (Figure 4) is directly tied to the abrupt increase in water vapor transport from the Pacific Ocean by way of the Gulf of California (Adams and Comrie (1997)). Within the NAM season, the occurrence of thunderstorms is closely linked to monsoon surge events that produce periods of peak precipitable water (see, for example, Watson and López (1994), Higgins et al. (2004), Yang et al. (2017)). Strong synoptic forcing is an important element of water vapor flux for numerous monsoon surge events that produce extreme rainfall and flooding.

To examine storm structure, motion and size for flash flood producing storms we carried out storm tracking analyses of 3-D reflectivity fields derived from KICX volume scan reflectivity data for 360 storm days. Lagrangian analyses are based on the TITAN

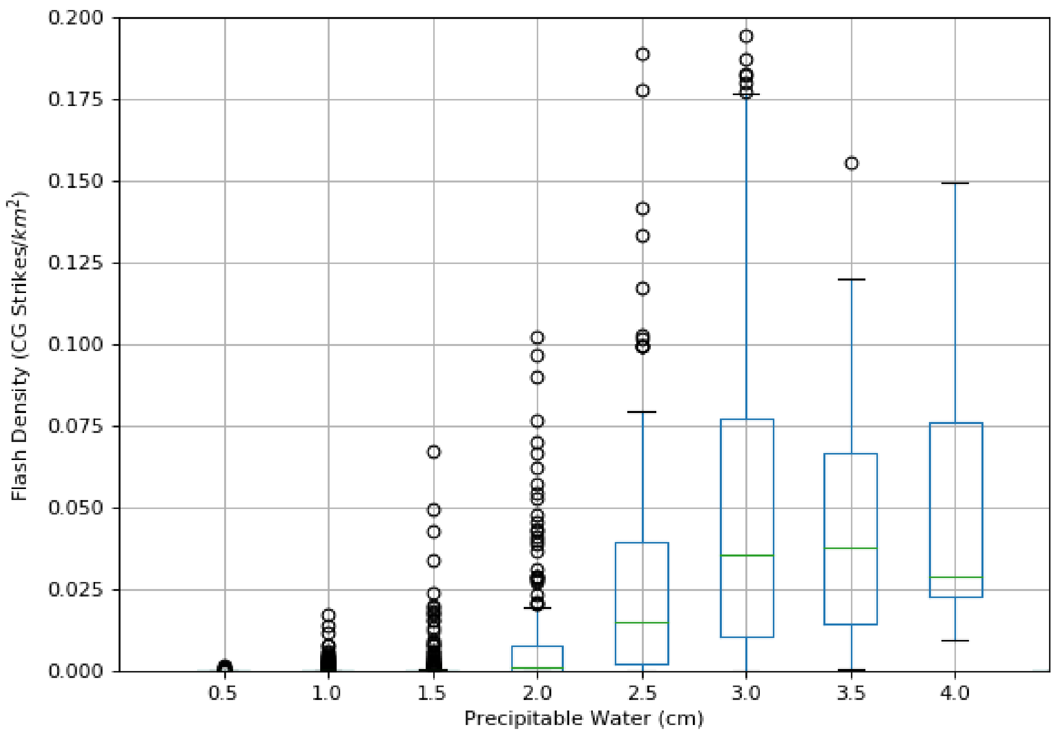

Figure 5. Daily flash density boxplots conditioned on precipitable water (in cm). Precipitable water bins cover 0.5 cm (the 3.0 cm bin, for example, includes days with precipitable water between 2.75 and 3.25 cm) Precipitable water measurements are from the Page, Arizona GPS (Global Positioning System) precipitable water station.

storm tracking algorithms (Section 2). A reflectivity threshold of 45 dBZ and volume threshold of 5 km^3 were used to identify storm elements.

Storm motion on flash flood days is predominantly from southwest to northeast (Figure 6) for the three months of the North American Monsoon season. The wind roses in Figure 6 reflect motion for storm elements with echo top height greater than 8.5 km.

Storm motion from southwest to northeast is most tightly concentrated for storms with the largest speeds (Figure 6). The median storm speed for the NAM season is 12 $km\ h^{-1}$ and the 0.9 quantile storm speed is 32 $km\ h^{-1}$ (Figure 7).

There are rare storm elements, like those in the 14 September 2015 storm, with storm speeds greater than 50 $km\ h^{-1}$. The 14 September 2015 Hildale storm was similar to flash flood producing storms in the region in terms of storm direction, but on the upper bound of storm speed. Storm motion from southwest to northeast reflects steering level winds that are associated with transport from the source of moisture - the Pacific Ocean to the southwest of the region.

The climatology of storm motion shows a pronounced seasonal transition from July through September. The predominant direction of motion in July is from the southwest, but there is a population of storms that depart from the norm, including storms with relatively small speeds covering all directions of motion. August is a transition month, including a contribution of storms deviating from southwest flow (like July) and a population of high storm speed events (like September). During September, when short-wave troughs moving from the northwest extend into the southwestern US, virtually all storms move from southwest to northeast.

Superimposed on the general southwest to northeast motion of storms for the region is geographic variability in mean storm motion for flash flood days (Figures 8 and 9). Mean motion vectors were computed from tracked storm elements with echo top height greater than 8.5 km. There are minima in storm speed over mountainous terrain and maxima over low elevation regions. Average storm speeds have a local maximum upwind of Short Creek and local minima in the headwater high-elevation regions of the North Fork and East Fork Virgin Rivers. The Glen Canyon region has an elongated zone of mean storm speeds greater than 27 $km\ h^{-1}$ (Figure 9). The are large contrasts in mean storm speed for the headwater portions of the Escalante and Paria River basins, relative to downstream portions of the drainage basins (Figure 9).

The median value of storm area for storm elements with echo top height of 8.5 km is 18 km^2 (Figure 7). The 0.9 quantile of storm area is 50 km^2. There is only modest variation in storm area distribution over the NAM season, in contrast to storm motion. Storm scale is one of the principal determinants of scale-dependent flood response in the study region, as discussed in detail below. Upscale growth of storms as they move away from peak elevations is modest compared with major flood-producing storms along the Front Range of the Rockies (see Javier et al. (2007) for additional discussion). Organization of convection into long lines is rare. In Section 5, we will see, however, that organized thunderstorms have contributed to extreme flooding in the study region.

Like storm size, and unlike storm motion, the distribution of maximum reflectivity values shows relatively little seasonal and geographic contrast. The median value of maximum reflectivity for storm elements with echo top height of 8.5 km is 55 dBZ (Figure 7), a value that typically indicates the presence of some hail. The 0.9 quantile of maximum reflectivity for flash flood days is 62 dBZ. Fewer than 1 in 100 storm elements on flash flood days have maximum reflectivity values that reach 70 dBZ - the 14 September 2015 Hildale storm is one.

4 The 14 September 2015 Storms and Floods

The Short Creek watershed (Figure 10) is located in one of the most remote areas in the conterminous US. The lower watershed of Short Creek includes the paired communities of Hildale, Utah and Colorado City, Arizona, which are divided by the Utah - Arizona boundary. Two thunderstorms passed over Short Creek on 14 September 2015 (Figure 11). For the first storm, which took a more easterly path, rainfall in Short Creek began around 2005 UTC (2:05 PM, Mountain Daily Time [MDT]) and ended by 2030 UTC. Rainfall in Maxwell Canyon for the second storm began at approximately 2215 UTC - the duration of rainfall over Maxwell Canyon was likely more than 10 minutes but less than 20. This second storm was the principal agent of catastrophic flooding in Maxwell Canyon and downstream in Short Creek. We will refer to this storm as the Hildale Storm, covering its entire life cycle from approximately 2130 UTC to 2345 UTC. The chronology of catastrophic flooding in Short Creek is closely tied to the structure and evolution of the Hildale Storm during the 20-minute time window from 2210 - 2230 UTC (Figure 12).

The first storm produced a significant flash flood in Short Creek and multiple cars waited at a low-water crossing of Short Creek until the peak receded. The second peak came down the Maxwell Canyon tributary and washed the waiting cars into Short Creek, resulting in 13 of the fatalities from the storm. Shortly after the second peak in Short

Creek swept through Hildale and Colorado City, 7 hikers were killed in Keyhole Canyon (see Figures 10 and 11), a popular canyoneering site in Zion National Park, 20 km north of Hildale. The upstream drainage area of Keyhole Canyon is approximately 1 km^2. The Hildale storm was responsible for the Short Creek and Zion fatalities, along with a record flood peak in the East Fork Virgin River at a drainage area of 890 km^2.

Stage measurements on Short Creek made by the Mojave County Flood Control District in Colorado City, Arizona exhibited a sharp rise beginning at 2100 UTC in response to the first storm, with a peak stage of 3.64 feet at 2134 UTC (see Figure 10 for location). Stage decreased below 1 foot at 2245 UTC, which marks the beginning of contributions from the second storm. Over the next 15 minutes, stage increased rapidly reaching the flood peak of 6.67 feet at 2300 UTC. The stream gage was disabled at 2317 UTC, with stage having decreased to 4.08 feet. A rain gage, which is colocated with the Short Creek stream gaging station, reported the first measured rainfall for the second storm at 2218 UTC. For the 7-minute period from 2218 UTC until 2225 UTC, 12 mm were recorded for a 7-minute rainfall rate exceeding 100 $mm\ h^{-1}$. An additional 2 mm of rain were recorded over the next 4 minutes. The Short Creek station is at relatively low elevation, 1492 meters MSL, compared to the headwaters of Maxwell Canyon, which have peak elevations exceeding 2000 meters MSL. Much more intense rainfall occurred to the north and west of the Short Creek stream gaging station over the Maxwell Canyon tributary.

The Hildale Storm was a monsoon thunderstorm in an environment with strong synoptic forcing. An upper level trough off the coast of California promoted exceptionally strong water vapor transport into the southwestern US, with rapid increase in precipitable water preceding initiation of the Hildalle Storm (Figure 13). At 1800 UTC the vertically integrated water vapor flux from the Gulf of California into the southwestern US approached 500 $kg\ s^{-1}\ m^{-1}$ and precipitable water exceeded 30 mm along the Virgin River valley. Precipitable water increased rapidly over the region prior to 1800 UTC. For the Page, Arizona GPS station, observed precipitable water increased from 8 mm at 0000 UTC on September 13 to 20 mm at 0000 UTC on September 14, followed by a sharp increase to 30 mm by 0600 UTC. Precipitable water from the Las Vegas, Nevada sounding at 1200 UTC on September 14 was 31.8 mm, an increase of 5.8 mm from the 0000 UTC sounding (see Figure 3 for location of the Las Vegas sounding). The Las Vegas precipitable water peak of 31.8 mm has been exceeded on fewer than 20 days in September since 1948.

Extreme rainfall over Maxwell Canyon was associated with a storm that exhibited peaks in convective intensity for the storm, for the day and generally for the collection of flash flood producing storms in the region (Figure 14; compare with results in the previous section). The Hildale Storm initiated southwest of Maxwell Canyon at approximately 2130 UTC (Figure 11) and intensified rapidly after 2145 UTC, with maximum reflectivity values reaching 65 dBZ by 2152 UTC (Figure 14 top). Convective intensity of the storm increased during the 10 minutes leading up to initiation of heavy rainfall over Maxwell Canyon at approximately 2215 UTC. Maximum reflectivity of the storm remained above 65 dBZ from 2217 UTC until 2310 UTC, with peak values exceeding 70 dBZ. The peak echo top height, i.e. the highest elevation with a reflectivity greater than 45 dBZ, of 11.5 km occurred around 2225 UTC. The rapid increase in convective intensity around 2217 UTC occurred as the storm approached the Vermillion Cliffs.

The area of peak lightning flash density was associated with passage of storms over the Vermiliion Cliffs, which mark the western boundary of Maxwell Canyon (Figure 15). The lightning map shows that the sharp terrain gradient at the Vermillion Cliffs was an area of peak convective intensity for the Hildale storm. The storm total lightning field reflects the contributions from the two storms described above (tracks are shown in Figure 11). The lightning flash density for the day over Maxwell Canyon was more that twice the mean annual value (Figure 3).

The Hildale Storm was exceptional for its rapid motion, in sharp contrast to conceptual models of flash-flood producing storms (Doswell et al. (1996) and Schumacher (2009)). During the 20 minute period centered on heavy rainfall over Maxwell Canyon, storm speed exceeded 50 $km\ h^{-1}$, with a peak speed of of 62 $km\ h^{-1}$ at 2243 UTC (Figure 14 bottom). Storm speed for the Hildale Storm was large in comparison with other tracked storm elements on 14 September 2015; the median storm speed for tracked storm elements with echo top height exceeding 8.5 km was 30 $km\ h^{-1}$ with only 10% of storm elements having storm speeds exceeding 45 $km\ h^{-1}$. Like convective intensity, storm speed for the Hildale storm was also extreme relative to the sample of flash flood producing storms in the region during the period from 1998 - 2016 (as detailed in Section 3).

During the critical period of extreme rainfall from 2210 to 2230 UTC, storm area ranged from 50 to 60 km^2 (Figure 14 middle). Storm area was anomalously large for the storm, for the day and for the population of flash flood producing storm elements (Figure 7). Flood peak measurements for Maxwell Canyon and Short Creek suggest that the most extreme rainfall was concentrated in Maxwell Canyon, which has a drainage area that is smaller than the storm size. Characterizing the extreme nature of rainfall from the Hildale storm centers on determining where and when extreme rainfall occurred within the Hildale Storm, as depicted in Figure 12.

The Hildale storm exhibited cyclonic rotation in radar polarimetric fields and in Doppler velocity fields (but was not a supercell). Dynamical processes associated with rotational motion in supercells and mesovortices can contribute to extreme rainfall rates, as detailed in (Nielsen & Schumacher, 2018) and (Weijenborg et al., 2017). During the period of heavy rainfall over Maxwell Canyon (Figure 12) the hail core was located in the northwest portion of the storm, with a line of elevated reflectivity extending to the east of the hail core and a line of elevated reflectivity extending south of the hail core. The line extending south of the hail core moved cyclonically from southwest of the hail core to southeast of the hail core over the 15 minute period. The cyclonically rotating storm structure around the hail core is also illustrated in the the Doppler velocity fields from 2214 to 2227 UTC (Figure 12; middle column). Doppler velocity observations show that the hail core was located at the nose of a low-level inflow jet, i.e. a low level maximum in wind speed.

Motion of the Hildale storm was slightly to the left of the steering level winds from 2100 to 2230. In Figure 16, we show vertical wind profiles derived from Cedar City WSR-88D Doppler Velocity measurements using the Velocity Azimuth Display (VAD) algorithm. Wind speed ranged from 35 to 50 $km\ h^{-1}$ (10 - 14 $m\ s^{-1}$) and wind direction was near constant at 225 degrees (south - southwesterly wind). Motion for the Hildale storm was more northerly than the larger population of storms on 14 September (Figure 16). Dynamical effects associated with storm rotation and flow channeling in the Short Creek canyon may have contributed to storm motion. There was little change in steering winds from the time of the first storm to the second - contrast in motion was principally tied to dynamical controls of storm evolution.

The evolution of extreme rainfall from the Hildale Storm is best reflected in K_{DP} fields (Figure 12; right column), which suggest that the line of elevated reflectivity extending north to south of the hail core and along the western margin of the storm was the "source" of extreme rainfall over Maxwell Canyon. Elevated K_{DP} values at approximately 3 km AGL increased rapidly from 2206 to 2214 UTC, with a north-to-south oriented arc of values reaching 3 degrees km^{-1}. The line of elevated K_{DP} was located upwind of Maxwell Canyon, with the timing and orientation of the line consistent with extreme rainfall rates over the watershed during the period from 2015 to 2030 UTC (based on storm speed and elevation of the radar beam). Melting hail and liquid water shed from hail are likely sources of extreme rainfall over Maxwell Canyon (Romine et al. (2008)). Strong downdrafts associated with negative buoyancy from precipitation drag and evaporation of rain and melting of hail likely contributed to extreme rainfall rates over Maxwell Canyon.

The period of extreme rainfall indicated by elevated K_{DP} values was short-lived, forming shortly after 2200 UTC and diminishing after 2216 UTC (Figure 12). Although the K_{DP} signature of extreme rainfall decayed rapidly after the storm passed Maxwell Canyon, it redeveloped as the storm approached the East Fork Virgin River and Keyhole Canyon (Figure 17). Like flash flooding in Maxwell Canyon, extreme rainfall over Keyhole Canyon and the East Fork Virgin River was linked to a small region of elevated K_{DP} in close proximity to the hail core of the Hildale Storm. K_{DP} fields point to the paroxysmal nature of the Hildale Storm - multiple pulses of extreme rainfall rates, with weaker rainfall occurring between the rain pulses.

Polarimetric radar provides insights to the development of heavy rainfall, but it is difficult to determine surface rainfall rates based on measurements that are 3 km above the ground, especially for storms with rapid storm motion like the Hildale storm. We examine rainfall from the storm using simulations of flood response with the KINEROS-2 hydrologic model; analyses are designed to assess rainfall rates associated with peak discharge of 266 m^3 s^{-1} in the 5.3 km^2 Maxwell Canyon watershed during the 10-20 minute rainfall period. We implemented the KINEROS-2 model for Maxwell Canyon with parameters derived from GIS data layers using the AGWA algorithms (see Morin et al. (2006) and Goodrich et al. (2011) and Section 2 for additional details). We use a digital elevation model with 10-m resolution, land use map from National Land Cover Dataset with a spatial resolution of 30 m and soil attributes from the SSURGO dataset. The Manning roughness coefficient for channels is 0.035. The watershed has large slopes, with a mean slope of 70% and more than 2/3 of the watershed having slopes greater than 30%, based on 10 meter elevation data. Field inspection of the watershed in November 2016 indicated that virtually the entire upper watershed of Maxwell Canyon had erosive runoff from the storm. We do not attempt to distinguish spatially varying rainfall over the watershed (given the elevation of the beam and rapid storm motion, polarimetric radar measurements provide little guidance on the spatial distribution of rain over the 5 km^2 watershed). Field observations were also used to partition the watershed into channel and plane flow elements.

We used hydrologic modeling analyses to examine the rainfall rates required to produce a flood peak of 266 m^3 s^{-1} in Maxwell Canyon at a drainage area of 5.3 km^2. We assume that the channel of Maxwell Canyon was fully wetted (by the first storm) when rainfall initiated around 2215 UTC. Assuming a wet watershed and channel, the constant rainfall rate over a 15 minute period needed to produce a peak discharge of 266 m^3 s^{-1} in Maxwell Canyon is 215 mm h^{-1}. For 10 minute time interval, the constant rainfall rate increases to 280 mm h^{-1}. For 20 minute time interval, the rainfall rate decreases to 190 mm h^{-1}

Rainfall rates inferred from hydrologic model analyses are larger than the 100 mm h^{-1} rain rates at 7-minute time scale measured at the downstream Short Creek stream gaging station. As noted above, radar, lightning and peak discharge measurements all point to rainfall rates in Maxwell Canyon that were markedly larger than those at the low-elevation gaging station. The peak discharge measurement of 266 m^3 s^{-1}, combined with hydrologic modeling analyses points to rainfall rates over Maxwell Canyon exceeding 200 mm h^{-1} at time scales less than 15 minutes. A key assumption in assessing rainfall rates through these analyses is the accuracy of the peak discharge measurement; as noted in the introduction measurement error is a major problem for the most extreme floods.

Hydrologic modeling analyses for Maxwell Canyon provide general guidance on rainfall rates associated with peak discharge values around 270 m^3 s^{-1} for 5 km^2 watersheds. Flood peaks from small drainage areas can result in record flood peaks over much larger downstream watersheds. The Hildale storm was responsible for the flood of record in the

East Fork of the Virgin River at a drainage area of 890 km^2 (Figure 18; peak discharge of 98 m^3 s^{-1}) from a 26-year record. The rainfall-weighted flow distance (Smith et al. (2002)) to the basin outlet for the East Fork Virgin River decreased to a value close to 8 km at 2240 UTC as the Hildale storm passed through the lower portion of the drainage basin, consistent with the rapid rise and peak discharge shortly after 0000 UTC on September 15 (Figure 18).

The DPR rainfall field at 2245 UTC (Figure 18) shows a storm with large rainfall rates close to the basin outlet. Elevation of the radar beam and storm speed dictate that the rainfall distribution at 2245 UTC was shifted somewhat from the location shown in Figure 18, but the conclusion that extreme rainfall was concentrated close to the outlet clearly holds. The record flood in the East Fork Virgin River at a drainage area of 890 km^2 was produced by a storm that was more than an order of magnitude smaller than the watershed and passed through the watershed in less than 20 minutes.

5 Extreme Floods in the Colorado Plateau

In this section we examine the hydroclimatology of extreme floods in the Colorado Plateau through analyses of USGS flood records from Fort Pearce Wash, Kanab Creek, the Virgin River, the Paria River, the Dirty Devil River and the Escalante River (Figure 1). We revisit storm properties through analyses of major flood-producing storms in the Colorado Plateau, focusing on Lagrangian storm properties derived from radar observations. Our focus is on the upper tail of flood peaks, including floods ranging from 10-year return interval to record floods. We compare storm properties to climatological features developed in Section 3 and to the distinctive properties of the 14 September 2015 Hildale Storm developed in the previous section.

Peak magnitudes for the 14 September 2015 flood decreased rapidly downstream of Short Creek. The downstream peak in Fort Pearce Wash at a drainage area of 3400 km^2 was almost an order of magnitude smaller than the upstream peaks in Maxwell Canyon at 5 km^2 and Short Creek at 50 km^2 scale (Figure 19; see Figure 1 for watershed location). The decrease in discharge from Short Creek to the Fort Pearce Wash gaging station resulted from flood peak attenuation and channel infiltration losses; the time of travel for the flood wave from Short Creek to Pearce Wash, approximately 11 hours, provides ample time for both (Figure 19).

The largest flood peaks in the 22-year record of Fort Pearce Wash occurred on 15 August 2003 and 16 July 2012. Both had magnitudes of approximately 270 m^3 s^{-1} (Figure 19), comparable to maximum discharge values from the 14 September 2015 storm in Maxwell Canyon and Short Creek from the Hildale Storm. The hydrograph for the July 2012 flood illustrates the common usage of "flash" as a verb for Colorado Plateau rivers. From a dry channel, discharge increased to the 270 m^3 s^{-1} peak in 40 minutes, with a similarly rapid falling limb of the hydrograph (Figure 19). The peak discharge and time to peak are virtually identical for the August 2003 flood.

Fort Pearce Wash flashed on 16 July 2012 in response to extreme rainfall rates from a severe thunderstorm that tracked through the region from 2200 to 2400 UTC (Figures 19 and 20). The rainfall-weighted flow distance to the basin outlet of Fort Pearce Wash was approximately 12 km at 2245 UTC (the time for which the rainfall rate field is shown in Figure 19). Like the record flood for the East Fork Virgin River on 14 September 2015, the rapid rise and fall of the Fort Pearce Wash hydrograph for the 16 July 2012 storm was produced by extreme rainfall rates during a short period from a storm near the basin outlet (Figure 19). The flood hydrology of southwestern US watersheds over a wide range of basin scales is dependent on hydrologic response to small areas of intense rainfall and channel infiltration losses in downstream channel segments.

Storm properties for the July 2012 flood in Fort Pearce Wash reprise many of the themes that emerge from analyses of the 14 September 2015 flood in its headwaters. Like the Hildale storm, the 16 July 2012 storm was large relative to flash flood producing storms in the study region, with 45 dBZ storm area exceeding 60 km^2. Also like the Hildale storm, the storm was rapidly moving, with storm speeds between 30 and 40 $km\ h^{-1}$, and motion was from southwest to northeast (Figure 19; compare also with the climatological analyses in Figures 7 and 8). K_{DP} signatures of extreme rainfall rates for the September 2015 Hildale Storm were also prominent features of the 16 July 2012 Fort Peace Wash storm (Figure 20); they were concentrated during a period of 15-20 minutes beginning at approximately 2240 UTC (Figure 20). The storm exhibited rotational signatures of a supercell thunderstorm, based on Doppler velocity observations and the NWS mesocyclone detection algorithm. Dynamical processes associated with storm rotation likely contributed to the extreme rainfall rates during the period from 2240 - 2300 UTC (see Nielsen and Schumacher (2018)). Like the Hildale Storm, the 16 July 2012 storm was an end-member on the convective intensity spectrum of flash flood producing storms.

Not all monsoon thunderstorms that produce flash floods move from southwest to northeast, as shown in Section 3 for a large sample of storms (Figures 6, 8 and 9). This result also holds when we restrict attention to extreme floods in the Colorado Plateau. Record and near-record floods in the Escalante River on 24 August 1998 (Figures 21), the upper Paria River on 19 August 2012 (Figures 22 and 23) and North Fork Virgin River on 12 July 2018 (Figure 24) were produced by thunderstorms that initiated along high elevation, headwater portions of the watershed and exhibited storm motion that differed markedly from the 14 September 2015 Hildale storm and 16 July 2012 Fort Pearce Wash storm.

The largest flood peak in the 62-year USGS stream gaging record of the Escalante River at 823 km^2 scale is the 130 $m^3\ s^{-1}$ peak from the 24 August 1998 storm (Figure 21). The storm producing the 1998 peak was a severe thunderstorm that formed along the drainage divide between the Escalante and Paria River basins. Over its life cycle the storm moved slowly to the east, away from the drainage divide. Small net storm motion resulted in heavy rainfall, intense lightning, flooding and landslides in the upper Escalante River basin (Figure 21 and NCEI Storm Events database). The most intense rainfall was concentrated in a small portion of the watershed and removed from the basin outlet; if the storm centroid had been 20 km further east, the flood peak at the USGS stream gaging station would likely have been much larger than 130 $m^3\ s^{-1}$.

Thunderstorms on 19 August 2012 (Figure 22) produced a flood peak of 214 $m^3 s^{-1}$ at the Paria River stream gage near Kanab, Utah at a drainage area of 1680 km^2. The August 2012 storm formed at high elevation close to the drainage divide and moved from northwest to southeast. There are large spatial gradients in mean motion of flash flood producing storms over the Paria watershed; motion of the 19 August 2012 storm is similar to mean motion in the area over which it passed (Figure 9). Average storm speeds are small in the upper Paria watershed. In the lower watershed mean storm speeds are large with a pronounced southwest to northeast orientation.

The upper Paria flashed in response to the 19 August 2012 storm with discharge increasing from near 0 to 214 $m^3 s^{-1}$ in 45 minutes. The August 2012 storm was a multicell storm, with an elongated region of elevated K_{DP} at 2046 UTC (Figure 22). Linear organization along the direction of motion together with storm motion down the watershed (see Morin et al. (2006)) contributed to the extreme nature of the flood peak.

The downstream peak for the Paria River at Lees Ferry, Arizona for the 19 August 2012 flood (see Figure 22 for location) was less than a third of the upstream peak near Kanab, again reflecting the prominent role of channel losses and flood peak attenuation in Colorado Plateau rivers (see Hereford (1986)). The distributions of flood peaks at the two Paria gaging stations for the period of overlapping records (1959 - 1973 and 2003

- 2015) are strikingly similar (Figure 23), despite the large difference in drainage area, 1680 km^2 versus 3680 km^2, highlighting the weak dependence of flood peak magnitudes on drainage area. The spatial contrasts in structure and motion of monsoon thunderstorms combine with open channel flow processes to determine flood peak properties over the Paria River basin, and more generally, over the Colorado Plateau.

Major flooding in the North Fork Virgin River on 12 July 2018 resulted from a thunderstorm that initiated over high elevations and moved slowly to the south (Figure 24). Discharge at the USGS stream gaging station, which has a drainage area of 891 km^2, rose from near 0 to the peak discharge of 153 $m^3\ s^{-1}$ in 30 minutes (Figure 25). The most extreme flooding, as reflected in locations of landslides, was concentrated in a small portion of the North Fork Virgin drainage basin and is contained within the area of maximum K_{DP} at 0200 UTC in Figure 24. Like the 14 September 2015 storm, the July 2018 storm exhibited rapidly varying K_{DP} signatures of extreme rainfall rates, with locations of peaks in K_{DP} paired with locations of hillslope damage and flooding. A 2-hour accumulation of 62 mm from a rain gage located due west of the storm track at 0215 UTC (denoted by a red star in Figure 24) has a return interval that is longer than 200 years. The distribution of hillslope damage and K_{DP} fields suggest that more extreme rainfall rates occurred around the storm location at 0200 UTC.

The record flood peak for the 92 years of observations from the North Fork Virgin River is 259 $m^3\ s^{-1}$ and occurred on 7 December 1966 (Butler and Munforff (1970)). The peak discharge of 646 $m^3\ s^{-1}$ at the downstream Virgin River station, which has a drainage area of 2480 km^2, is 70% larger than the second largest flood peak in a stream gaging record of more than 100 years. It is one of the largest flood peaks in the systematic USGS stream gaging record from the Colorado Plateau (Figure 2). Rainfall totals for the December 1966 storm were unprecedented. The 24-hour accumulation of 112 mm at Orderville, Utah on December 6 (Butler and Munforff (1970)) has a return interval of approximately 500 years (NOAA Atlas 14, Volume 1, Version 5). The 3-day total rainfall at Orderville was 184 mm. Not surprisingly, there are sharp contrasts in the timing of flood response between the December 1996 flood and the July 2018 flood (Figure 25).

Winter storms are important flood agents for large watersheds in the Colorado Plateau, both in the current climate and during the past several millennia (Ely (1997)). The December 1966 flood peaks were produced by a powerful extratropical cyclone affecting the region from 5 - 7 December 1966 (Butler and Munforff (1970)). The main difference between the December 1966 storm and the July 2018 storm is the spatial extent of extreme rainfall; the December 1966 storm produced heavy rainfall over the entire Virgin River basin; the July 2018 storm produced extreme rainfall over a small portion of the North Fork Virgin River basin.

The differences between fall/winter storms and monsoon thunderstorms are not, however, as absolute as they may seem. Although much of the rainfall from the December 1966 storm was likely stratiform, radar observations (see Plate 2 of Butler and Munforff (1970)) suggest that convection may have contributed peak rainfall rates in some locations. The flood peak of 259 $m^3\ s^{-1}$ on the North Fork Virgin River followed a rapid rise produced by an organized region of heavy rainfall (Figure 25 and Plate 2 of Butler and Munforff (1970)). The downstream rise to the 646 $m^3\ s^{-1}$ peak in the Virgin River was even sharper. As noted in Section 3, the seasonally varying properties of monsoon thunderstorms from July through September are tied to the increasing frequency of synoptic scale disturbances in September. Similar issues arise in assessing the changing structure and evolution of storms that produce extreme floods through the fall and winter seasons.

The largest flood peak among the Colorado Plateau USGS stream gaging stations is the 1014 $m^3\ s^{-1}$ peak which occurred on 7 October 2006 in the Dirty Devil River at a drainage area of 10,800 km^2 (Figure 2; see Figure 1 for basin location). Although the storm lies outside of the monsoon season, it produced severe thunderstorms with extensive lightning (Figure 26); large hail and tornadoes were also reported during the storm period (NCEI Storm Events database). Thunderstorm frequency during October, as shown in Figure 4, is quite low.

The October 2006 flood was the product of an extratropical system with a cutoff low west of the study region. Synoptic scale forcing for the October 2006 storm resulted in organization of rainfall into broken lines of convection with associated regions of stratiform rain. Lines of convection generally moved eastward and embedded storm elements tracked from south to north, resulting in heavy rainfall over the region for a period of more than 24 hours (Figure 27). As the lightning map indicates, heavy rain was most closely tied to intense convection in the southern portion of the region, with weaker convection making more prominent contributions in the northern portion of the region, including the Dirty Devil River basin. Extreme rainfall and flooding also occurred in the Escalante River basin, principally downstream of the USGS stream gaging station. Flooding in the Escalante below the USGS stream gaging station was the most extreme since at least 1983. Sediment that had been deposited in the lower Escalante River during the 1983 Colorado River flood in Lake Powell (see Greenbaum et al. (2014)) was excised.

The largest flood peaks in Kanab Creek at 502 km^2 drainage area during the past 5 decades have been produced by extratropical systems during September. Heavy rainfall on 27 September 2014 was organized by a cutoff low centered in California; flooding and flash flooding extended from southern Arizona through Utah into the northern Rocky Mountains of Wyoming, Idaho and Montana.

Synoptic forcing on 27 September 2014 resulted in organization of rainfall into broken lines of convection (Figure 28). The storms produced near-record daily lightning counts for the study region, with peak flash densities exceeding 5 CG strikes km^{-2}. As the cutoff low moved slowly to the east, lines of convection shifted eastward, with heaviest rainfall over the North Fork Virgin River between 1530 and 1630 UTC and heaviest rainfall over Kanab Creek from 1630. - 1830 UTC (Figure 28).

Although the system moved from west to east, tracked storm elements moved rapidly from southwest to northeast, consistent with the climatology of flash flood producing storms during September (Figure 6). Organization of rainfall into broken lines of convection resulted in multiple storm elements producing rainfall in both Kanab Creek and the North Fork Virgin River (the location of a flash flood fatality during the event: see NCEI Storm Events Database). The most intense storm elements that passed through Kanab Creek, like the one shown at 1752 UTC (Figure 28), did not, however, track close to the outlet of Kanab Creek. Organization of rainfall into broken lines of convection and persistence of heavy rainfall over multiple hours contributed to flooding in Kanab Creek. The absence of a storm element tracking close to the basin outlet constrained the potential for extreme flooding at the USGS stream gaging station.

The recent history of flooding in Kanab Creek has been relatively quiet - the 84 $m^3\ s^{-1}$ flood peak on 28 September 2014 reflects the most extreme flooding during the past 50 years. Kanab Creek has seen much larger floods and is a setting in which periods with elevated frequency of extreme floods have been documented. Woolley notes that "on August 30, 1882, a terrific flood swept down Kanab Creek Canyon and literally swamped the town. This was followed by similar cloudburst floods each summer until 1886. In that period of 5 years the channel was changed almost beyond the comprehension of even those who saw it. Its depth increased by 50 feet or more and its width by about 200 feet in places" (Woolley (1946)). Kanab Creek provides one of the most striking examples of arroyo formation during the late 19th century.

Analyses of the arroyo problem have pointed to extended periods (multi-year to multi-decadal) with elevated frequency of extreme floods throughout the Colorado Plateau

(Graf (1983), Webb and Hereford (2001), Antevs (1952), Hereford and Webb (1992), Balling Jr. and Wells (1990), Higgins and Shi (2000) and Harvey and Pederson (2011)). Paleoflood studies point to clustering of extreme floods over millennial time scales. The Colorado Plateau has experienced multiple periods of elevated flood frequency during the past 1000 years (Webb and Baker (1988) and Webb et al. (1988)).

Palehydrologic reconstructions in the Escalante River (Webb et al. (1988)) include a 600 m^3 s^{-1} peak close to the current stream gaging location from a "cloudburst" storm on 27 August 1932 (Woolley (1946) and Webb et al. (1988)). Paleoflood peaks approaching 2000 m^3 s^{-1} (Figure 2) have been reported for the lower Escalante River at drainage areas between 3000 and 4000 km^2 (Webb et al. (1988) and Enzel et al. (1993)). These are the largest flood peaks for basins with drainage area greater than 100 km^2, but not for smaller basins - the 14 September 1974 Eldorado Canyon hailstorm produced a peak larger than 2000 m^3 s^{-1} at 50 km^2 (Figure 2).

There is a large gap between the 130 m^3 s^{-1} peak in the Escalante River on 24 August 1998 and the 600 m^3 s^{-1} peak in August 1932 and an even larger distance to the 2,000 m^3 s^{-1} paleoflood peaks in the lower Escalante. "Organization" of rainfall in space and time, as illustrated by the December 1966, October 2006 and September 2014 storms provides one avenue for bridging the gap. The paroxysmal precipitation of the desert, as illustrated by the 14 September 2015 Hildale Storm and the 14 September 1974 Eldorado Canyon Storm provides another. Understanding the climatology of extreme floods in the Colorado Plateau will likely require a deeper understanding of both paths.

6 Summary and Conclusions

The major findings of this paper are the following:

- The 14 September 2015 Hildale Storm in southern Utah, which resulted in 20 flash flood fatalities, provides the quintessential example of the paroxysmal precipitation of the desert. Polarimetric radar measurements suggest that two 10-20 minute periods of extreme rainfall rates during the 2 hour life cycle of the hailstorm resulted in catastrophic flash flooding. Both periods are characterized by K_{DP} signatures of extreme rainfall. Similar K_{DP} signatures characterized multiple storms that have produced record and near-record flood peaks in Colorado Plateau watersheds.
- The Hildale Storm developed a cyclonic structure with a line extending east of the hail core and a cyclonically rotating line that initially extended south from the hail core. The southward-oriented line developed the elevated K_{DP} signature that was the precursor to extreme rainfall rates over Maxwell Canyon. Melting hail and liquid water shed from hail are likely sources of extreme rainfall rates over Maxwell Canyon and Keyhole Canyon. Negative buoyancy associated with precipitation drag and evaporation of rain and melting of hail may have contributed to downdraft enhancement of extreme rainfall rates. Hydrologic modeling analyses indicate that 15-minute rainfall rates in excess of 200 mm h^{-1} are needed to produce a flood peak of 266 m^3 s^{-1} in Maxwell Canyon at a drainage area of 5 km^2.
- For the sample of flash flood producing storms during the period from 1998 - 2016, the 14 September 2015 hailstorm was among the most extreme in terms of convective intensity. The Hildale storm was also exceptional for its storm speed, which exceeded 50 km h^{-1}, placing it in the extreme upper tail of storm speeds for flash flood events in the region. Slow storm speed or small net storm motion are among the most common attributes of extreme flash flood events (Doswell et al. (1996)). Extreme storm speed for the Hildale storm sharpens the focus on extreme short-term rainfall rates as the key element of extreme flooding.

- Synoptic scale forcing was an important element of water vapor flux into Arizona and southern Utah, preceding initiation of the Hildale Storm. Precipitable water increased steadily from less than 10 mm to 30 mm in the 24 hours preceding storm initiation. A rear inflow jet created by the Hildale storm combined with the strong southwest to northeast water vapor flux over the region to create an environment with exceptionally strong water vapor flux to the storm.
- There is a pronounced seasonal cycle in NAM thunderstorm characteristics, including an evolving climatology of storm motion. The NAM season is dominated by storms that move from southwest to northeast, but July includes a significant population of storms with motion deviating from the norm. The seasonal cycle is also characterized by an increasing frequency of baroclinic disturbances in September, when southwest to northeast storm motion is most prominent.
- "Sooner or later the cloudburst visits every tract", as Gilbert noted, but every tract is unique in the paroxysmal nature of rainfall. The climatology of thunderstorms in the Southwestern US study region exhibits spatial heterogeneities that are tied to terrain and large-scale features of storm environment. Superimposed on terrain controls of storm initiation are the seasonal and spatial variations in storm motion. Record and near-record flood peaks in Kanab Creek, Virgin River, Paria River and Escalante River illustrate the striking terrain controls on storm structure and motion for monsoon thunderstorms.
- The distribution of flood peak magnitudes in Colorado Plateau watersheds is weakly dependent on basin scales, relative to other regions of the US. Flood response is closely linked to the spatial scale of thunderstorms, which have typical sizes ranging from 10 to 50 km^2. Large floods peaks in many watersheds are produced by "small", monsoon thunderstorms that pass close to the basin outlet. Flood peak attenuation and channel infiltration losses also contribute to an environment in which small storms play a major role in flood frequency for much larger watersheds.
- Organization of rainfall in time and space contributes to extreme flood peaks from Fall - Winter storms. The December 1966, October 2006 and September 2014 flood episodes illustrate settings in which multiple storm elements and sub-watersheds contributing synchronously to produce extreme flooding.

Acknowledgments

This research was supported by the United States-Israel Bi-national Science Foundation (Grant BSF-2016953) and the National Science Foundation (Grant EAR-1632048). The authors gratefully acknowledge constructive suggestions from Vic Baker and John England. NLDN data were provided by the NASA Lightning Imaging Sensor (LIS) instrument team and the LIS data center via the Global Hydrology Resource Center (GHRC) located at the Global Hydrology and Climate Center (GHCC), Huntsville, Alabama, through a license agreement with Global Atmospherics (now Vaisala), Inc (GAI).

References

Adams, D. K., & Comrie, A. C. (1997). The North American Monsoon. *Bulletin of the American Meteorological Society*, *78*(10), 2197 - 2213.

Antevs, E. (1952). Arroyo-cutting and filling. *Journal of Geology*, *60*, 375 - 385.

Baker, V. R. (2008). Paleoflood hydrology: Origin, progress, prospects. *Geomorphology*, *101*, 1 -13.

Balling Jr., R. C., & Wells, S. G. (1990). Historical rainfall patterns and arroyo activity within the Zuni River drainage basin, New Mexico. *Annals of the Association of American Geographers*, *80*, 603 - 617.

Berwick, V. K. (1962). *Floods in Utah, Magnitude and Frequency* (Circular No. 457). U. S. Geological Survey.

Bieda, S. W., Castro, C. L., Mullen, S. L., Comrie, A. C., & Pytlak, E. (2009). The Relationship of Transient Upper-Level Troughs to Variability of the North American Monsoon System. *Journal of Climate*, *22*, 4213 - 4227.

Bosart, L. F., Seimon, A., LaPenta, K. D., & Dickinson, M. J. (2006). Supercell tornadogenesis over complex terrain: the Great Barrington, Massachusetts tornado on 29 May 1995. *Weather and Forecasting*, *21*, 897- 921.

Butler, E., & Munforff, J. C. (1970). *Floods of December 1966 in Southwestern Utah* (USGS Water-Supply Paper No. 1870-A). Washington D. C.: U.S. Geological Survey.

Corbosiero, K. L., Dickinson, M. J., & Bosart, L. F. (2009). The contribution of eastern North Pacific tropical cyclones to the rainfall climatology of the southwestern United States. *Monthly Weather Review*, *137*, 2415 - 2435.

Costa, J. E., & Jarrett, R. D. (2008). *An evaluation of selected extraordinary floods in the united states reported by the u. s. geological survey and implications for future advancement of flood science* (Vol. Scientific Investiations Report 2008-5164). U.S. Geological Survey.

Cotton, W. R., Bryan, G. H., & van den Heever, S. C. (2010). *Storm and cloud dynamics* (2nd edition. ed.) (No. 775 pg.). Academic Press.

Crippen, J. R., & Bue, C. D. (1977). *Maximum floodflows in the conterminous United States* (U.S. Geological Water Supply Paper No. 1887). USGS.

Cummins, K. L., & Murphy, M. J. (2009). An overview of lightning locating systems: History, techniques, and data uses, with an in-depth look at the U.S. NLDN. *IEEE Transactions on Electromagnetic Compatibility*, *51*(3), 499–518.

Cummins, K. L., Murphy, M. J., Bardo, E. A., Hiscox, W. L., Pyle, R. B., & Pifer, A. E. (1998). A combined TOA/MDF technology upgrade of the US National Lightning Detection Network. *Journal of Geophysical Research - Atmospheres*, *103*(D8), 9035–9044.

Cunha, L. K., Smith, J. A., Baeck, M. L., & Krajewski, W. F. (2013). An early performance evaluation of the NEXRAD dual polarization radar rainfall estimates for urban flood applications. *Weather and Forecasting*, *28*, 1478 - 1497.

Deierling, W., & Petersen, W. A. (2008). Total lightning activity as an indicator of updraft characteristics. *Journal of Geophysical Research*, *113*(D16210). (doi:10.1029/2007JD009598)

Dixon, M., & Wiener, G. (1993). TITAN - Thunderstorm Identification, Tracking, Analysis, and Nowcasting - A radar-based methodology. *Journal of Atmospheric and Oceanic Technology*, *10*(6), 785–797.

Doswell, C. A., Brooks, H. E., & Maddox, R. A. (1996). Flash flood forecasting: An ingredients-based methodology. *Weather and Forecasting*, *11*(4), 560-581.

Ely, L. L. (1997). Response of large floods in the southwestern United States to climatic variations in the late Holocene. *Geomorphology*, *18*, 175 - 201.

Ely, L. L., Enzel, Y., & Cayan, D. R. (1994). Anomalous North Pacific atmospheric circulation and large winter floods in the southwestern United States. *Journal of Climate*, *7*(6), 977 - 987.

Enzel, Y., Ely, L. L., House, K., & Baker, V. R. (1993). Paleoflood evidence for a natural upper bound to flood magnitudes in the Colorado River basin. *Water Resources Research*, *29*(7), 2287 - 2297.

Etheredge, D., Gutzler, D. S., & Pazzaglia, F. J. (2004). Geomorphic response to seasonal variations in rainfall in the southwest United States. *Geological Society of America Bulletin*, *116*(5/6), 606 - 618.

Gilbert, G. K. (1877). *Geology of the Henry Mountains* (Tech. Rep.). Washington D. C.: U. S. Geographical and Geological Survey of the Rocky Mountain Region.

Gilbert, G. K. (1890). *Lake Bonneville* (Tech. Rep.). Washington D. C.: U.S. Geological Survey.

Glancy, P. A., & Harmsen, L. (1975). A Hydrologic Assessment of the September 14, 1974, Flood in Eldorado Canyon, Nevada. *U. S. Geological Survey Profes-*

sional Paper 930, 28 pp.
Goodrich, D. C., et al. (2011). AGWA: The automated geospatial watershed assessment tool to inform rangeland management. *Rangelands*, *33*(4), 41-47.
Graf, W. L. (1983). The arroyo problem - paleohydrology and paleohydraulics in the short term. In K. G. Gregory (Ed.), *Backgrounds to paleohydrology* (p. 279 - 302). New York: John Wiley & Sons.
Greenbaum, N., Harden, T. M., Baker, V. R., Weisheit, J., Cline, M. L., Porat, N., . . . Dohrenwend, J. (2014). A 2000 year natural record of magnitudes and frequencies for the largest Upper Colorado River floods near Moab, Utah. *Water Resources Research*, *50*, 5249 - 5269.
Hales, J. E. (1975). A severe southwestern desert thunderstorm: 19 August 1973. *Monthly Weather Review*, *103*, 344 - 351.
Harvey, J. E., & Pederson, J. L. (2011). Reconciling arroyo cycle and paleoflood approaches to late holocene alluvial records in dryland streams. *Quaternary Science Reviews*, *30*, 855 - 866.
Hereford, R. (1986). Modern alluvial history of the Paria River drainage basin, southern Utah. *Quaternary Research*, *25*, 293 - 311.
Hereford, R., & Webb, R. H. (1992). Historic variation of warm-season rainfall, southern Colorado Plateau, southwestern USA. *Climatic Change*, *22*(3), 239 - 256.
Higgins, R. W., & Shi, W. (2000). Dominant Factors Responsible for Interannual Variability of the Summer Monsoon in the Southwestern United States. *Journal of Climate*, *13*, 759 - 775.
Higgins, R. W., Shi, W., & Hain, C. (2004). Relationships between Gulf of California Moisture Surges and Precipitation in the Southwestern United States. *Journal of Climate*, *17*, 2983 - 2997.
Higgins, R. W., Yao, Y., & Wang, X. L. (1997). Influence of the North American monsoon system on the U.S. summer precipitation regime. *Journal of Climate*, *10*, 2600–2622.
Hitchens, N. M., & Brooks, H. E. (2013). Preliminary investigation of the contribution of supercell thunderstorms to the climatology of heavy and extreme precipitation in the US. *Atmospheric Research*, *123*(206 - 210).
Hjalimarsom, H. W., & Thomas, B. E. (1992). New Look at Regional FloodFrequency Relations for Arid Lands. *Journal of Hydarulic Engineering*, *116*(868 - 886).
Hu, H., & Dominguez, F. (2015). Evaluation of Oceanic and Terrestrial Sources of Moisture for the North American Monsoon Using Numerical Models and Precipitation Stable Isotopes. *Journal of Hydrometeorology*, *16*, 19 - 35.
Hubbert, J., Bringhi, V. N., Carey, L. D., & Bolen, S. (1998). CSU-CHILL Polarimetric radar measurements from a severe hail storm in Eastern Colorado. *Journal of Applied Meteorology*, *37*, 749–775.
Javier, J. R. N., Smith, J. A., England, J., Baeck, M. L., Steiner, M., & Ntelekos, A. A. (2007). Climatology of extreme rainfall and flooding from orographic thunderstorm systems in the upper Arkansas River basin. *Water Resources Research*, *43*(W10410). (doi:10.1029/2006WR005093)
King, T. S., & Balling Jr., R. C. (1994). Diurnal variations in Arizona monsoon lightning data. *Monthly Weather Review*, *122*, 1659–1664.
Koenig, T. A., Bruce, J. L., O'Connor, J. E., McGee, B. D., Holmes, R. R., Hollins, R., . . . Peppler, M. C. (2016). *Identifying and Preserving High-Water Mark Data* (Surface-Water Techniques No. Chapter 24). U.S. Geological Survey.
Kumjian, M. R. (2013). Principles and applications of dual-polarization radar. *Journal of Operational Meteorology*, *1*(19 - 21), 226 - 274.
Kumjian, M. R., Lebo, Z. J., & Morrison, H. C. (2015). On the mechanisms of rain formation in an idealized supercell storm. *Monthly Weather Review*, *143*, 2754 - 2773.

Kumjian, M. R., & Ryzhkov, A. V. (2008). Polarimetric Signatures in Supercell Thunderstorms. *Journal of Applied Meteorology and Climatology*, *47*, 1940 - 1961.

Lang, T. J., & Rutledge, S. A. (2002). Relationships between convective storm kinematics, precipitation, and lightning. *Monthly Weather Review*, *130*, 2492–2506.

Leopold, L. B. (1942). Areal extent of intense rainfalls, New Mexico and Arizona. *Transactions of the American Geophysical Union*, *23*, 558 - 563.

Leopold, L. B. (1946). Two intense local floods in New Mexico. *Transactions of the American Geophysical Union*, *27*(4), 535 - 539.

Leopold, L. B. (1976). Reversal of erosion cycle and climate change. *Quaternary Research*, *6*, 557 - 562.

Luong, T. M., Castro, C. L., Chang, H. I., Lahmers, T., Adams, D. K., & Ochoa-Moya, C. A. (2017). The More Extreme Nature of North American Monsoon Precipitation in the Southwestern United States as Revealed by a Historical Climatology of Simulated Severe Weather Events. *Journal of Applied Meteorology and Climatology*, *56*, 2509 - 2529.

Maddox, R. A., Canova, F., & Hoxit, L. R. (1980). Meteorological characteristics of flash floods over the western United States. *Monthly Weather Review*, *108*, 1866 - 1877.

Maddox, R. A., McCollum, D. M., & Howard, K. W. (1995). Large-scale patterns associated with severe summertime thunderstorms over central Arizona. *Weather and Forecasting*, *10*, 763 - 778.

Maddox, R. A., Zhang, J., Gourley, J. J., & Howard, K. W. (2003). Weather radar coverage over the contiguous united states. *Weather and Forecasting*, *17*, 927 - 934.

Mazon, J. J., Castro, C. L., Adams, D. K., Chang, H., Carillo, C. M., & Brost, J. J. (2016). Objective climatological analysis of extreme weather events during the North American monsoon. *Journal of Applied Meteorology and Climatology*, *55*, 2431 - 2450.

Morin, E., Goodrich, D. C., Maddox, R. A., Gao, X. G., Gupta, H. V., & Sorooshian, S. (2006). Spatial patterns in thunderstorm rainfall events and their coupling with watershed hydrological response. *Advances in Water Resources*, *29*(6), 843-860. doi: {10.1016/j.advwatres.2005.07.014}

Morin, E., Maddox, R. A., Goodrich, D. C., & Sorooshian, S. (2005). Radar Z-R Relationship for Summer Monsoon Storms in Arizona. *Weather and Forecasting*, *20*(4), 672 - 679.

Nielsen, E. R., Herman, G. R., Tournay, R. C., Peters, J. M., & Schumacher, R. S. (2015). Double impact: when both tornadoes and flash floods threaten the same place and time. *Weather and Forecasting*, *30*, 1673 - 1693.

Nielsen, E. R., & Schumacher, R. S. (2018, 3009). Dynamical Insights into Extreme Short-Term Precipitation Associated with Supercells and Mesovortices. *Journal of the Atmospheric Sciences*, *75*(DOI: 10.1175/JAS-D-17-0385.1), 2983.

Orville, R. E. (2008). Development of the National Lightning Detection Network. *Bulletin of the American Meteorological Society*, *89*(2), 180–190.

Pascale, S., Boos, W. R., Bordoni, S., Delworth, T. L., Kapnick, S. B., Murakami, H., ... Zhang, W. (2017). Weakening of the North American Monsoon with global warming. *Nature Climate Change*, *7*, 806 - 813.

Petersen, W. A., & Rutledge, S. A. (1998). On the relationship between cloud-to-ground lightning and convective rainfall. *Journal of Geophysical Research*, *103*, 14025–14040.

Powell, J. W. (1895). *Exploration of the colorado river and its canyons* (No. 458 pg.). New York: Dover Publications.

Reap, R. M., & MacGorman, D. R. (1989). Cloud-to-ground lightning: Climatological characteristics and relationships to model fields, radar observations, and

severe local storms. *Monthly Weather Review*, *117*, 518–535.
Rogash, J. A., & Racy, F. (2002). Some Meteorological Characteristics of Significant Tornado Events Occurring in Proximity to Flash Flooding. *Weather and Forecasting*, *17*, 155 - 159.
Romine, R. S., Burgess, D. W., & Wilhelmson, R. B. (2008). A Dual-Polarization-Radar-Based Assessment of the 8 May 2003 Oklahoma City Area Tornadic Supercell. *Monthly Weather Review*, *136*, 2849 - 2870.
Ryberg, K. R., Goree, B. B., Williams-Sether, T., & Mason Jr., R. R. (2017). *The U.S. Geological Survey Peak-Flow File Data Verification Project* (Scientific Investigations Report No. 2017-5119). U. S. Geological Survey.
Ryzhkov, A. V., Kumjian, M. R., Ganson, S. M., & Zhang, P. (2013). Polarimetric Radar Characteristics of Melting Hail. Part II: Practical Implications. *Journal of Applied Meteorology and Climatology*, *52*, 2871 - 2886.
Schaffner, M., Unkrich, C., Goodrich, D., Lericos, T., Czyzyk, S., & Pierce, B. (2016). *Modeling hydrologic events in a semi-arid basin of complex terrain using a real time distributed model: Short creek at colorado city, arizona* (Western Region Technical Attachment No. 16-03). National Weather Serice.
Schumacher, R. S. (2009). Mechanisms for Quasi-Stationary Behavior in Simulated Heavy-Rain-Producing Convective Systems. *Journal of the Atmospheric Sciences*, *66*, 1543 - 1568.
Smith, J. A., & Baeck, M. L. (2015). "Prophetic Vision, Vivid Imagination": The 1927 Mississippi River Flood. *Water Resources Research*, *51*, 9964 - 9994.
Smith, J. A., Baeck, M. L., Meierdiercks, K. L., Nelson, P. A., Miller, A. J., & Holland, E. J. (2005). Field studies of the storm event hydrologic response in an urbanizing watershed. *Water Resources Research*, *41*(10), W10413(15).
Smith, J. A., Baeck, M. L., Morrison, J. E., Sturdevant-Rees, P., Turner-Gillespie, D. F., & Bates, P. D. (2002). The regional hydrology of extreme floods in an urbanizing drainage basin. *Journal of Hydrometeorology*, *3*(3), 267–282.
Smith, J. A., Baeck, M. L., Zhang, Y., & Doswell III, C. A. (2001). Extreme rainfall and flooding from supercell thunderstorms. *Journal of Hydrometeorology*, *2*, 469–489.
Smith, J. A., Cox, A. A., Back, M. L., Yang, L., & Bates, P. (2018). Strange Floods: The Upper Tail of Flood Peaks in the US. *Water Resources Research*, *54*, 6510 - 6542.
Tapia, A., Smith, J. A., & Dixon, M. (1998). Estimation of convective rainfall from lightning observations. *Journal of Applied Meteorology*, *376*, 1497–1509.
Thomas, B. E., Hjalimarsom, H. W., & Waltemeyer, S. D. (1994). *Methods for Estimating Magnitude and Frequency of Floods in the Southwestern US* (Open File Report No. 93-419). U. S. Geological Survey.
Thomas, B. E., & Lindskov, K. L. (1983). *Methods for Estimating Peak Discharge and Flood Boundaries of Streams in Utah* (Water Resources Investigation No. 4129). U. S. Geological Survey.
Villarini, G., & Smith, J. A. (2013). Spatial and temporal variability of cloud-to-ground lightning over the continental U.S. during the period 1995–2010. *Atmospheric Research*, *124*, 137 - 148.
Vivoni, E. R., Bowman, R. S., Wyckoff, R. L., Jakubowski, R. T., & Richards, K. E. (2006). Analysis of a monsoon flood event in an ephemeral tributary and its downstream hydrologic effects. *Water Resources Research*, *42*(W03404). (doi:10.1029/2005WR004036)
Watson, A. I., Holle, R. L., & Lopez, R. E. (1994). Cloud-to-ground lightning and upper-air patterns during bursts and breaks in the southwest monsoon. *Monthly Weather Review*, *122*, 1726 - 1739.
Watson, A. I., López, R. E., & Holle, R. L. (1994). Diurnal cloud-to-ground lightning patterns in Arizona during the Southwest Monsoon. *Monthly Weather Review*, *122*, 1716–1725.

Watson, A. I., & López, R. L. H. R. E. (1994). Cloud-to-ground lightning and upper-air patterns during bursts and breaks in the Southwest Monsoon. *Monthly Weather Review*, *122*, 1726–1739.

Webb, R. H., & Baker, V. R. (1988). Changes in hydrologic conditions related to large floods on the Escalante River, south-central Utah. In V. Singh (Ed.), *Regional Flood Frequency Analysis* (p. 306 - 320). Dordrecht.

Webb, R. H., & Hereford, R. (2001). Floods and geomorphic change in the southwestern US: an historical perspective. In *Seventh Federal Interagency Sedimentation Conference* (p. IV 30 - IV 37).

Webb, R. H., O'Connor, J. E., & Baker, V. R. (1988). Paleohydrologic reconstruction of flood frequency on the Escalante River, south-central Utah. In V. R. Baker (Ed.), *Flood Geomorphology* (p. 403 - 418). Wiley-Interscience.

Weijenborg, C. J., Chagnon, J., Friedrichs, P., Gray, S., & Hense, A. (2017). Coherent evolution of potential vorticity anomalies associated with deep moist convection. *Quarterly Journal of the Royal Meteorological Society*, *143*(704), 1254 - 1267.

Wood, K. M., & Ritchie, E. A. (2013). An updated climatology of tropical cyclone impacts on the southwestern United States. *Monthly Weather Review*, *141*, 4322 - 4336.

Wood, V. T., Brown, R. A., & Vasiloff, S. V. (2003). Improved detection using negative elevation angles for mountaintop WSR-88Ds. *Weather and Forecasting*, *18*, 393 - 403.

Woolley, R. R. (1946). *Cloudburst Floods in Utah 1850 - 1938* (Water Supply Paper No. 994). US Government Printing Office, Washinton DC: U.S. Geological Survey.

Yang, L., Smith, J. A., Baeck, M. L., Morin, E., & Goodrich, D. (2017). Flash Flooding in Arid/Semi-arid Regions: Dissecting the 19 August 2014 Flood over Arizona, Southwestern United States. *Journal of Hydrometeorology*, *18*, 3110 - 3124.

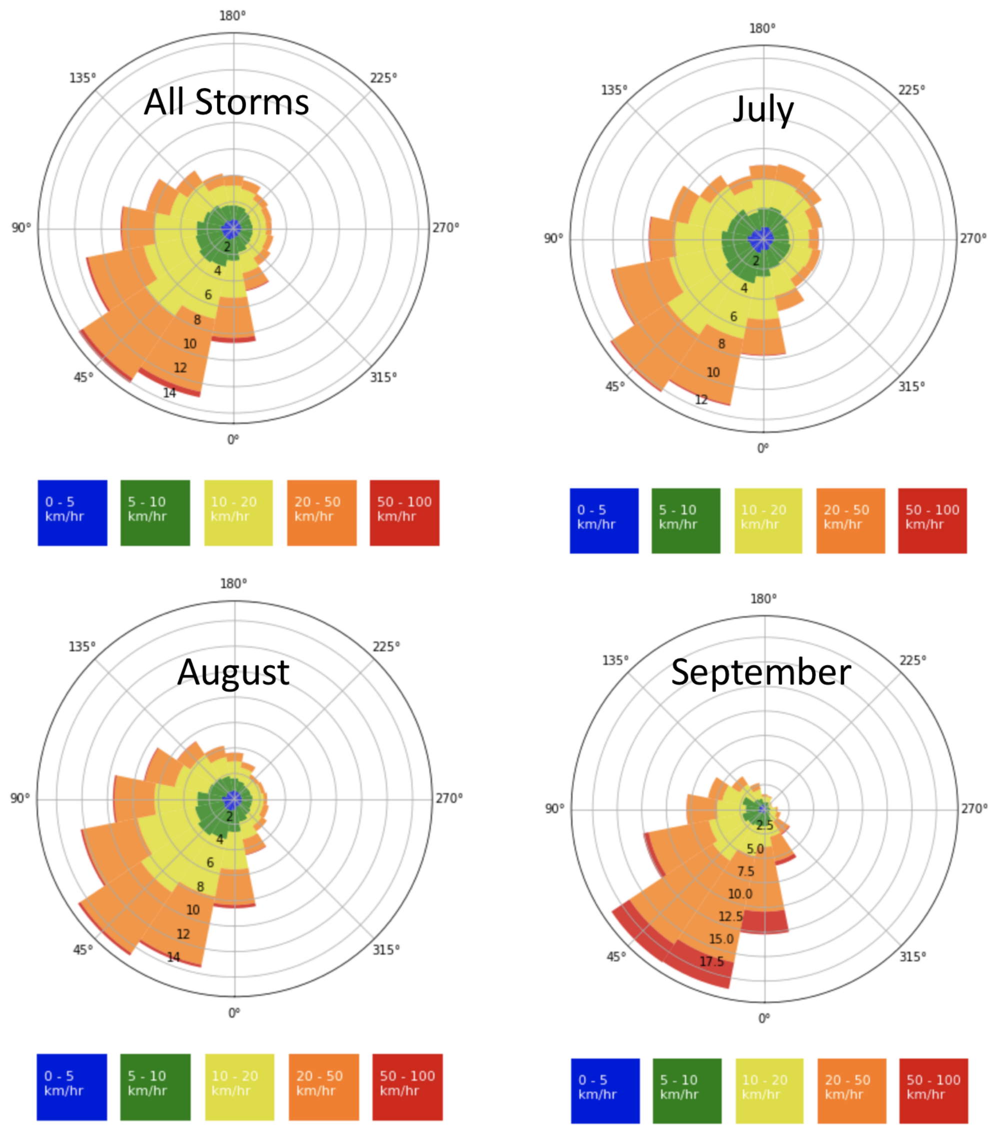

Figure 6. Windrose of storm motion and speed for flash-flood producing storms, 1998 - 2015 (tracked storm elements with 45 dBZ tops greater than 8.5 km); all storms (upper left), July (upper right), August (lower left) and September (lower right)

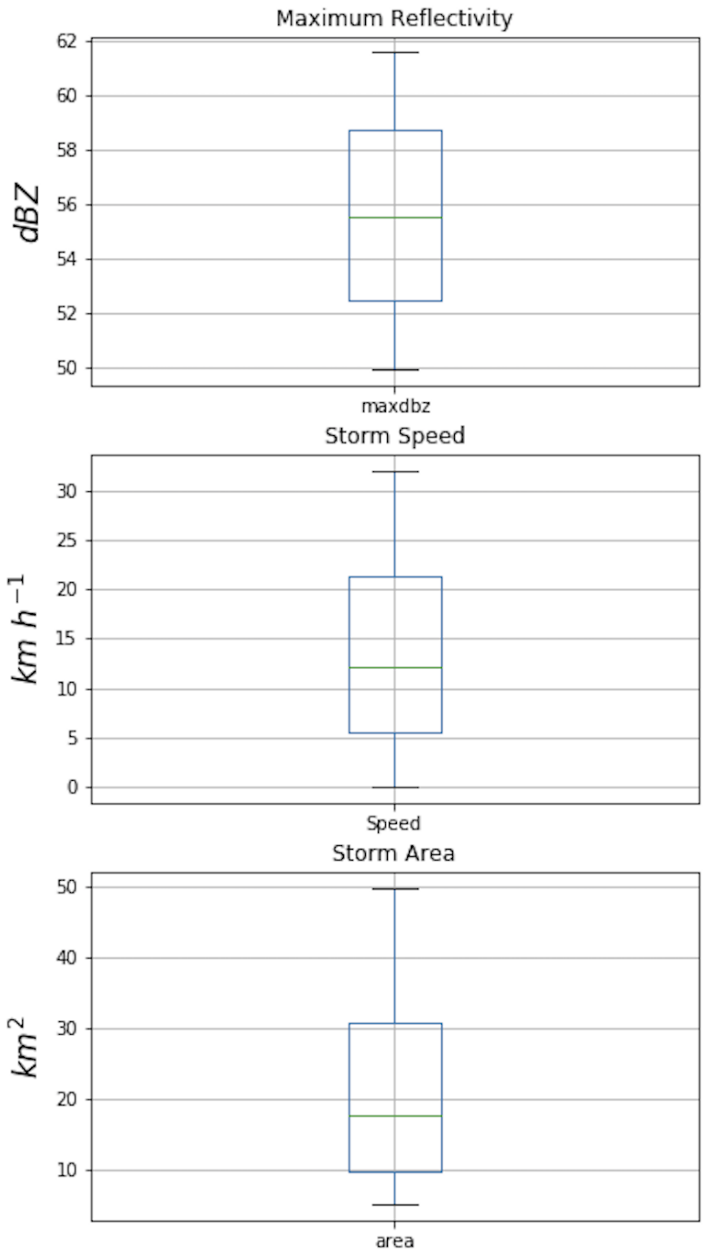

Figure 7. Box plots of maximum reflectivity (top), storm speed (middle) and storm area (bottom) for flash-flood producing storms, 1998 - 2015 (tracked storm elements with 45 dBZ tops greater than 8.5 km). Whiskers are for 0.1 and 0.9 quantiles.

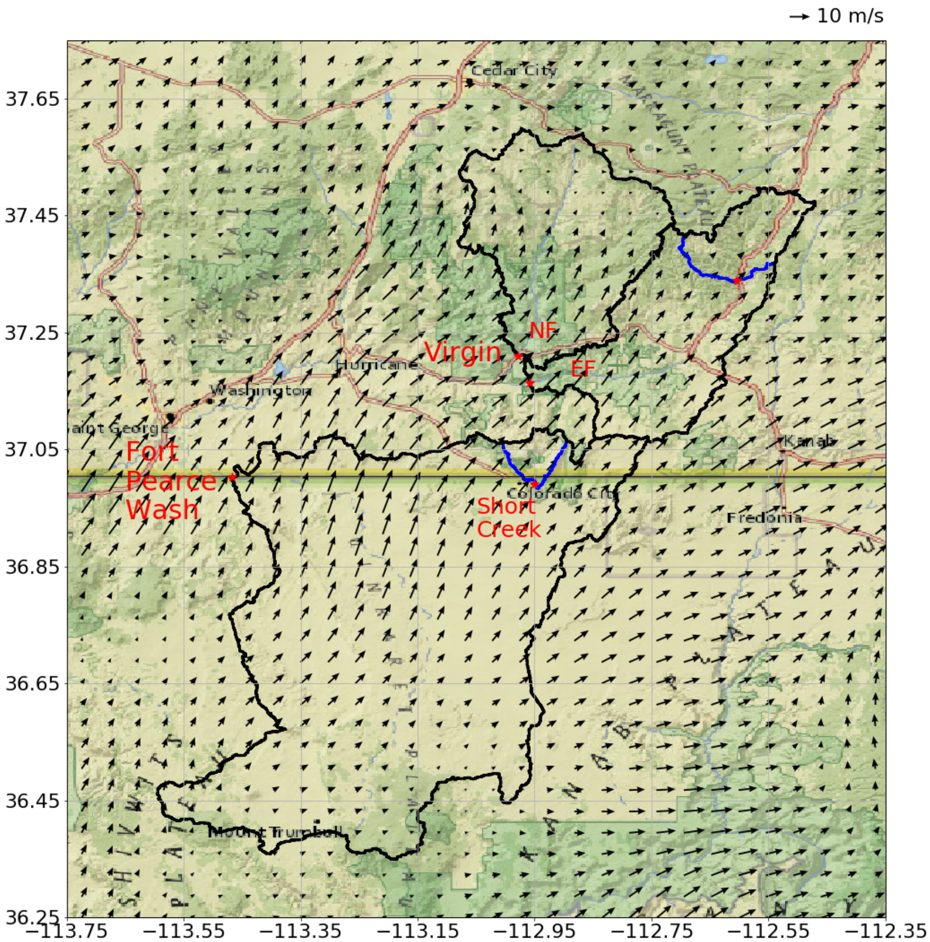

Figure 8. Mean storm motion vectors for flash-flood producing storms, 1998 - 2015 (tracked storm elements with 45 dBZ tops greater than 8 km); western region with Fort Pearce Wash (and Short Creek), East Fork Virgin and North Fork Virgin river basin boundaries.

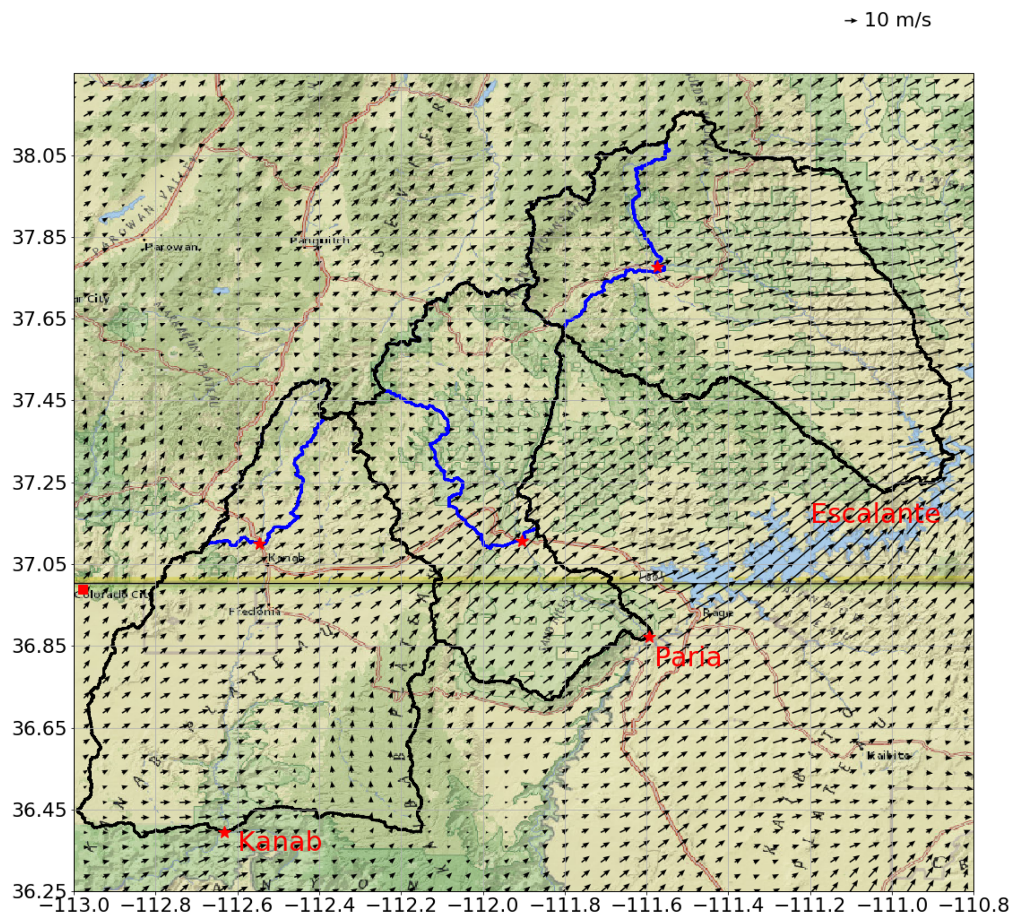

Figure 9. Mean storm motion vectors for flash-flood producing storms, 1998 - 2015 (tracked storm elements with 45 dBZ tops greater than 8 km); eastern region, with basin boundaries for Kanab Creek, the Escalante and the Paria River. Lake Powell (shown in blue) inundates Glen Canyon.

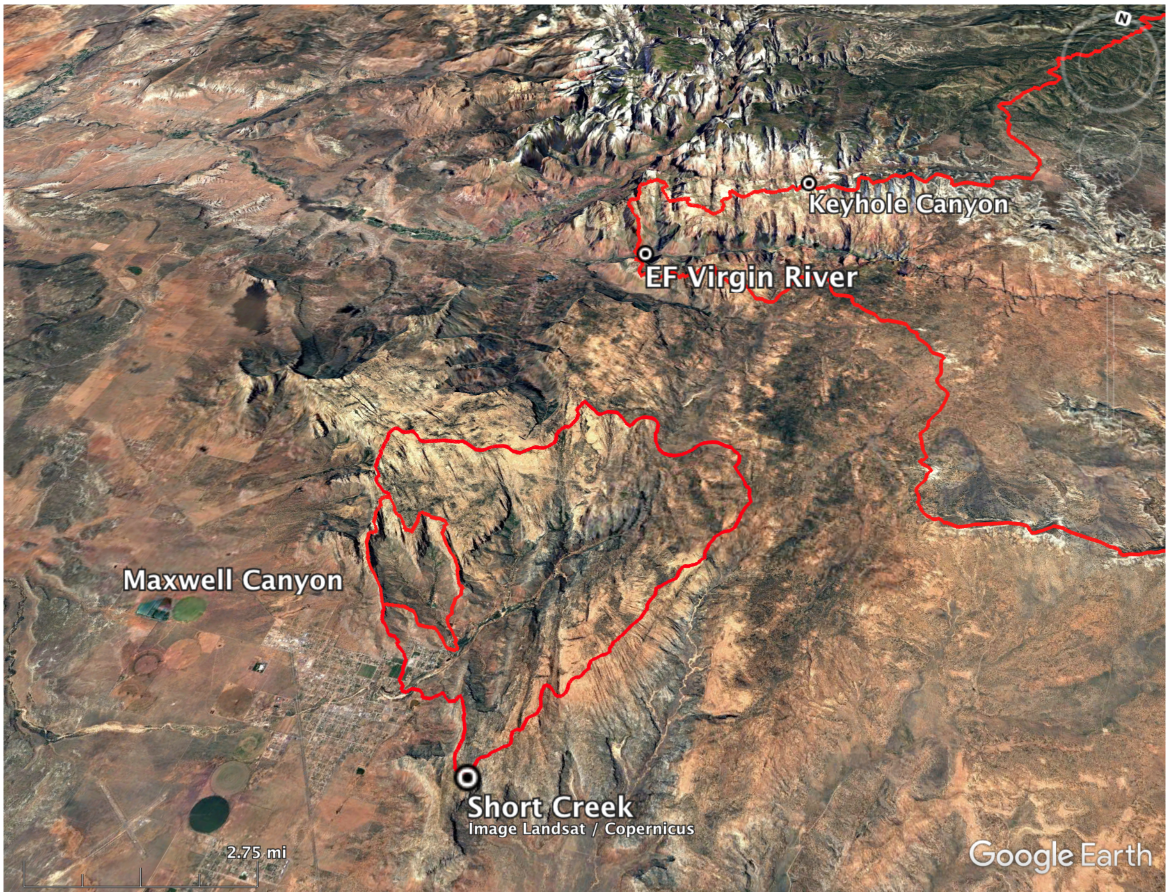

Figure 10. Short Creek, Maxwell Canyon and Virgin River study region. Basin boundaries of Maxwell Canyon and Short Creek are shown, along with a partial basin boundary for the East Fork Virgin River (outlet is marked by black circle). Keyhole Canyon is also marked by a black circle.

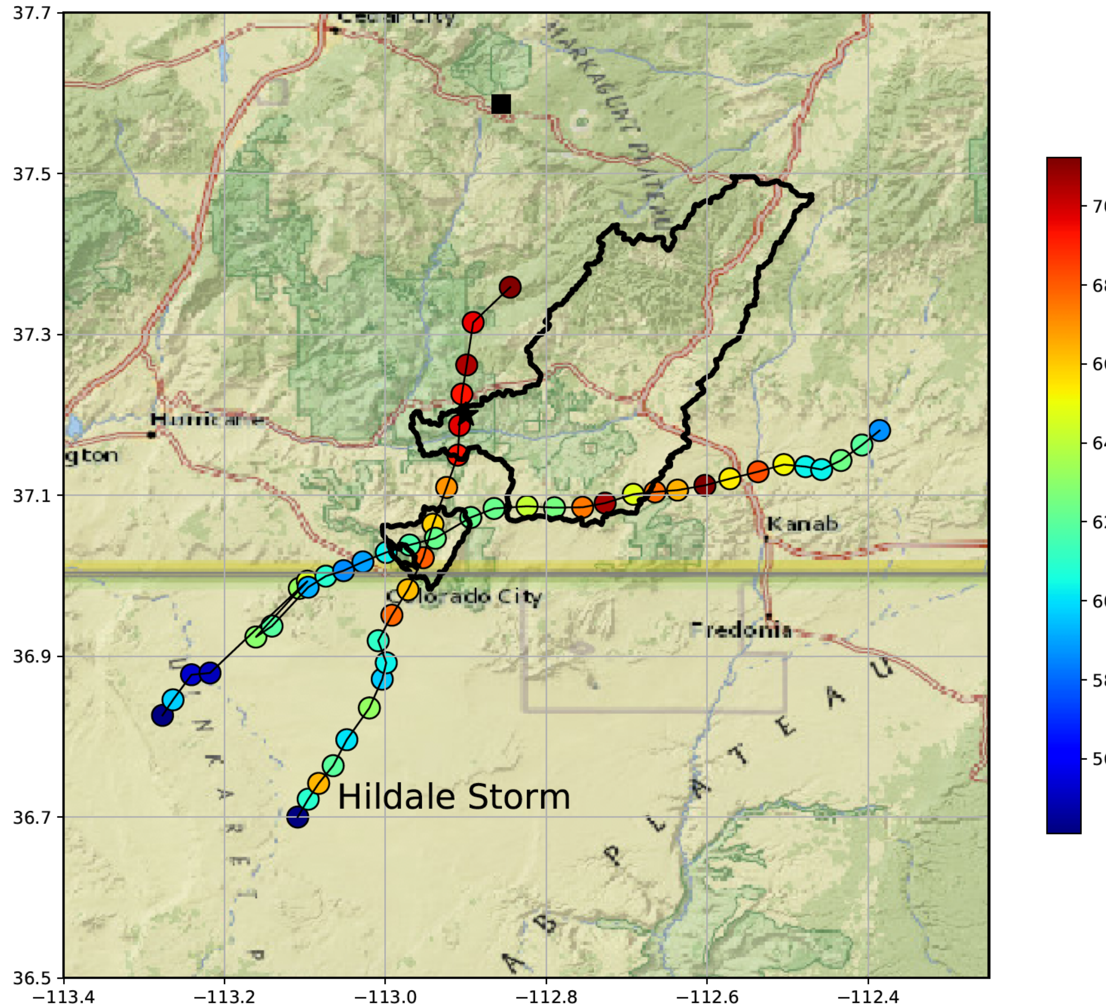

Figure 11. Tracks for the two storms that passed through Short Creek on 14 September 2015; the Hildale Storm is the second to pass through Short Creek. Points are color coded by maximum reflectivity (dBZ). The Short Creek and E. Fork Virgin River basin boundaries are outlined (see also Figure 10). Keyhole Canyon is marked by a black star and the KICX radar location is denoted by a black square.

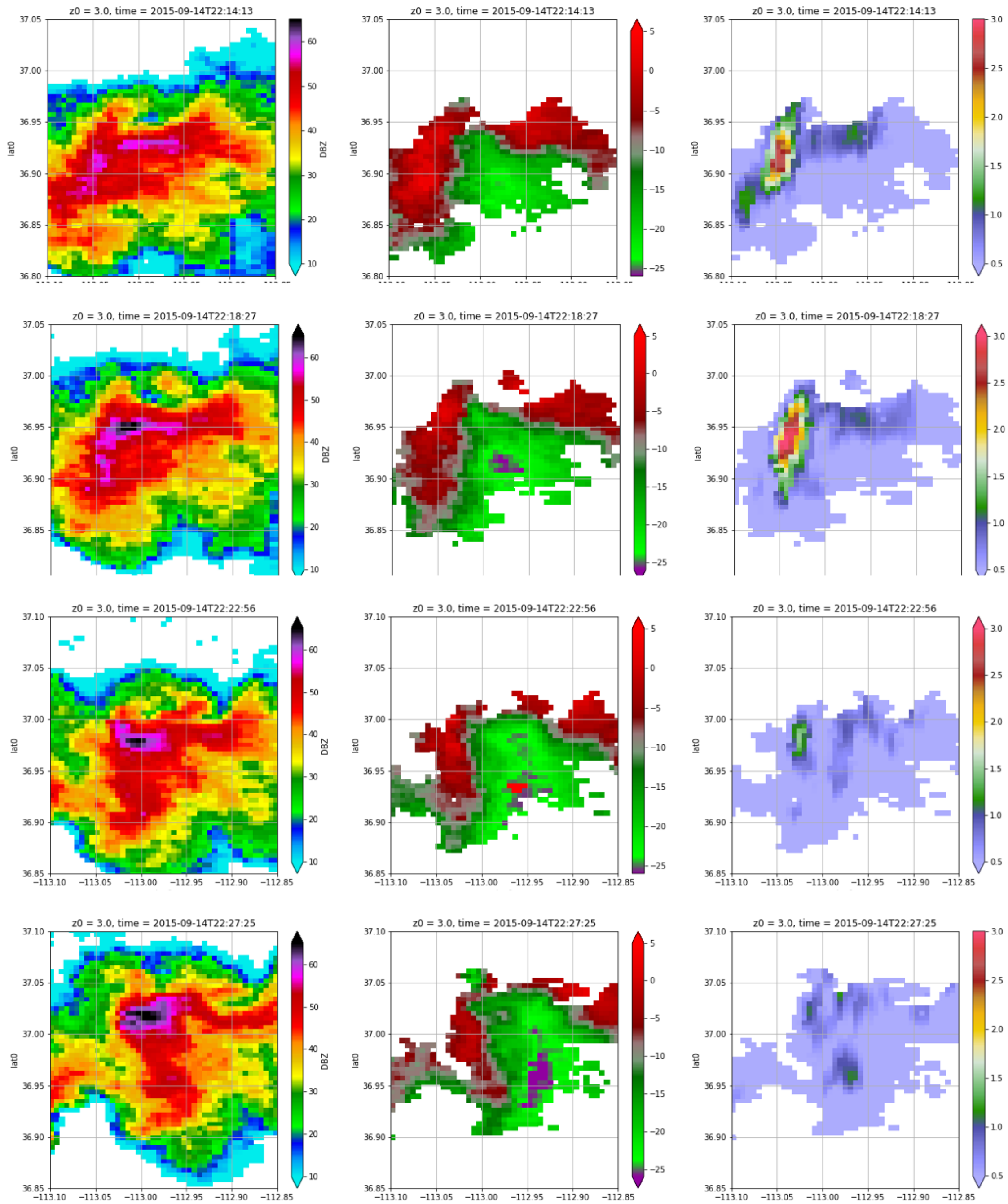

Figure 12. Reflectivity (left), Doppler velocity (middle) and specific differential phase shift (right) at 2214, 2218, 2222 and 2227 UTC (from top to bottom) on 14 September 2015 from the Cedar City WSR-88D.

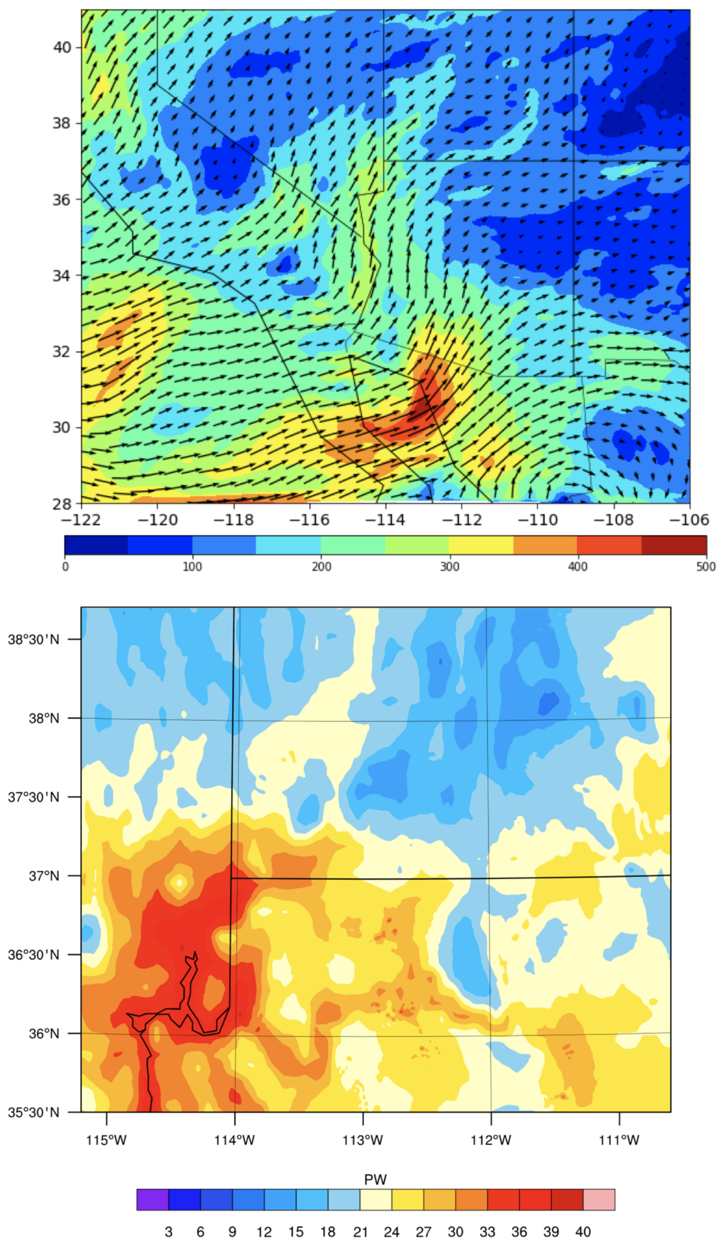

Figure 13. Vertically integrated water vapor flux ($kg\ s^{-1}\ m^{-1}$)at 1800 UTC on 14 September 2015 (top) from WRF simulation (outer domain). Arrows depict vertically integrated water vapor flux vector, with length proportional to magnitude of the flux. The color scale represents magnitude of the flux ($kg\ s^{-1}\ m^{-1}$). The bottom figure shows the precipitable water (mm) field at 1800 UTC for the inner domain.

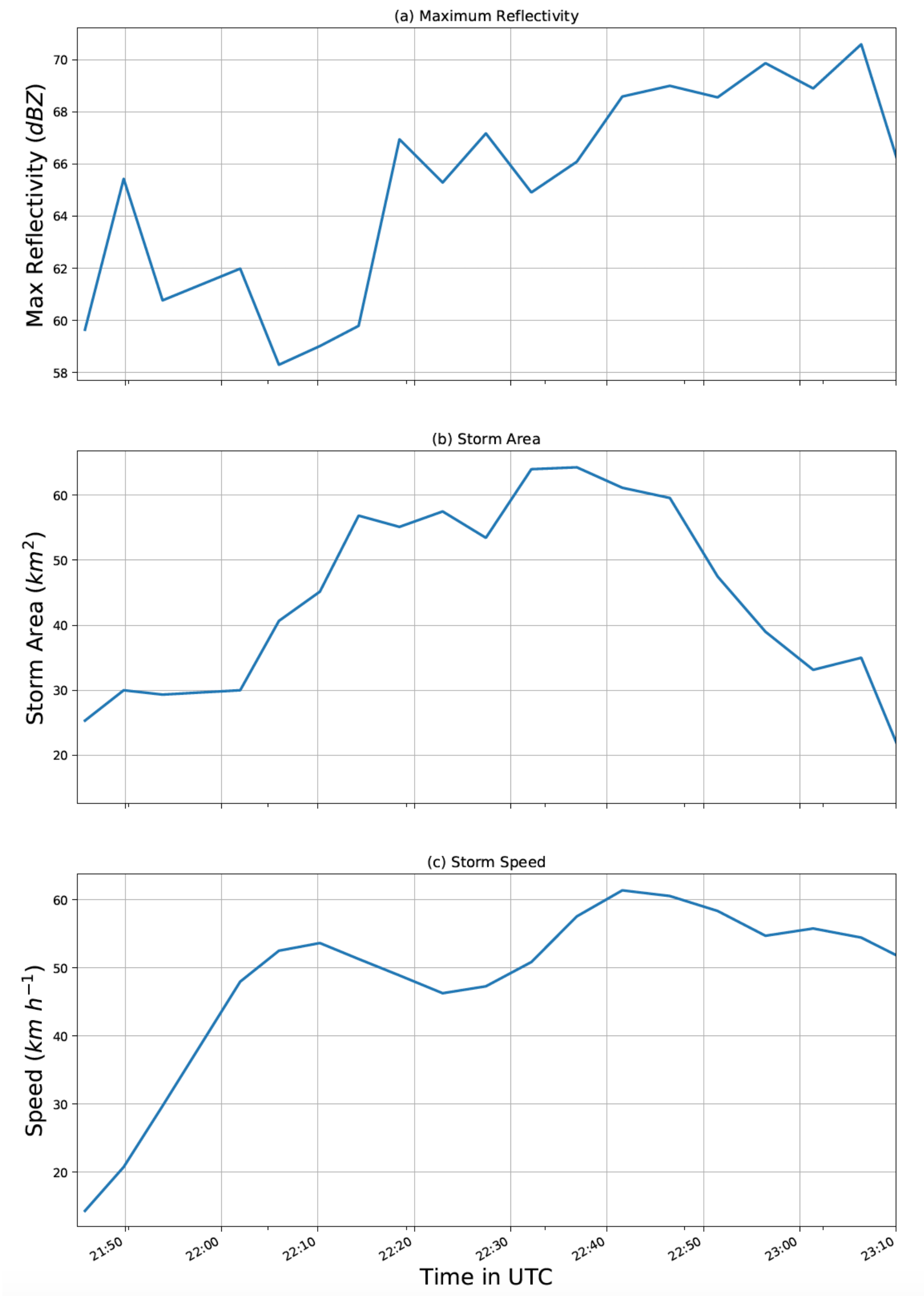

Figure 14. Time series of maximum reflectivity (dBZ; top), storm area (km^2; middle) and storm speed ($km\ h^{-1}$; bottom) for the 14 September 2015 Hildale Storm, based on TITAN storm tracking analyses (see also Figure 11).

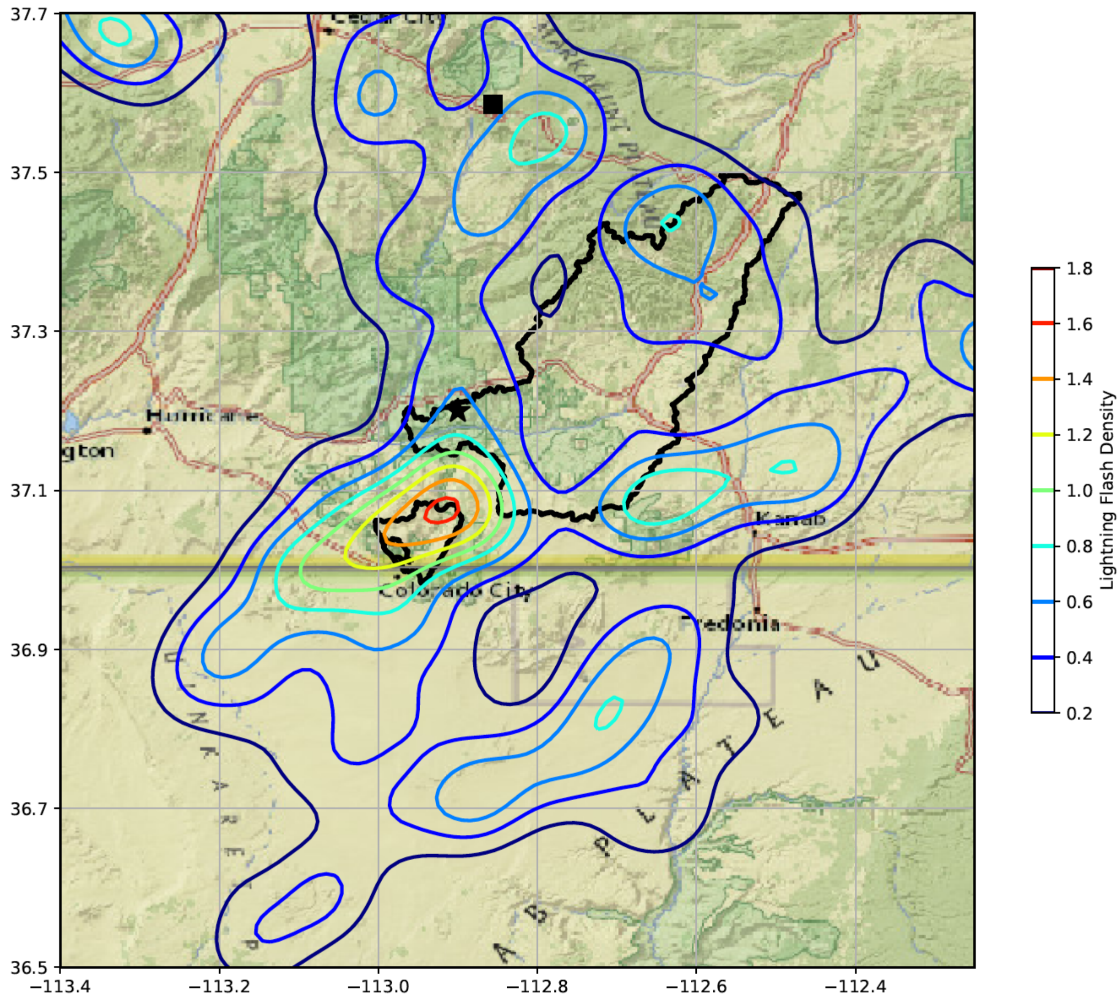

Figure 15. CG lightning flash density contours (CG strikes km^{-2}) for the 14 September 2015 storm. The Maxwell Canyon, Short Creek and E. Fork Virgin River basin boundaries are outlined. Keyhole Canyon is marked by a black star. The KICX radar location is denoted by a black square.

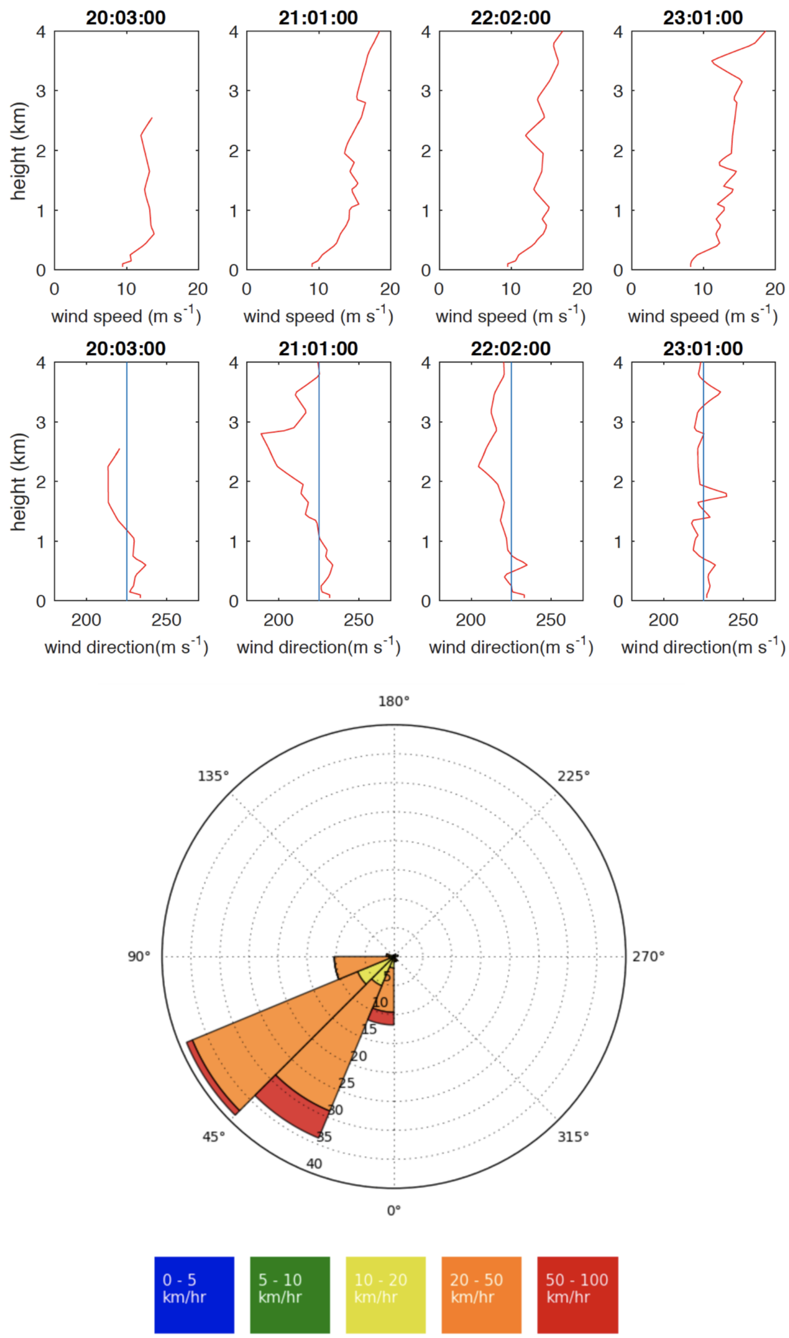

Figure 16. Wind profiles from KICX Velocity Azimuth Display (VAD) analyses from 2000 - 2300 UTC (top). Elevation is given in height above the radar; elevation of the radar is 3200 meters MSL. The vertical blue line for wind direction is 225 degrees (wind direction from south-west). Wind rose of storm direction and storm speed for all tracked storms on 14 September 2015 with tops greater than 8.5 km (bottom).

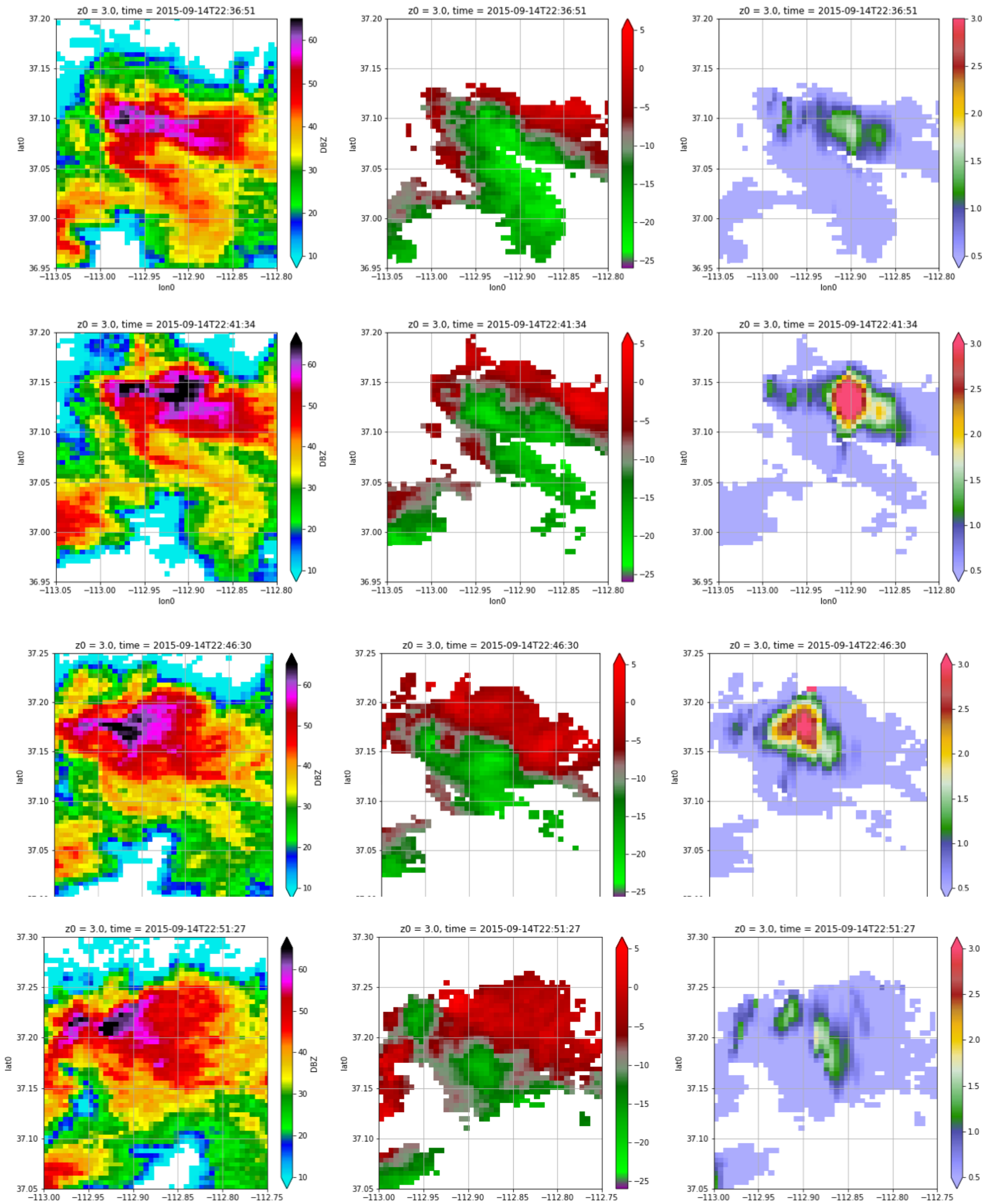

Figure 17. Reflectivity (left), Doppler velocity (middle) and specific differential phase shift (right) at 2236, 2241, 2246 and 2251 UTC (top to bottom) on 14 September 2015 from the Cedar City WSR-88D.

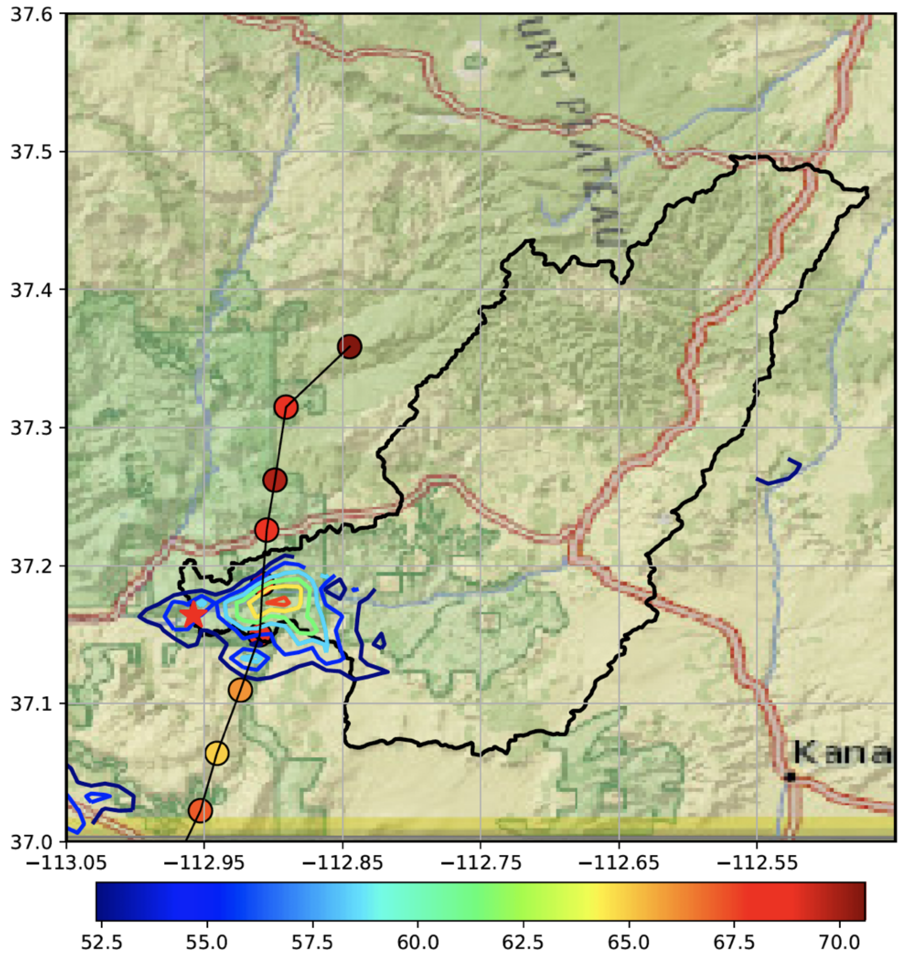

Figure 18. Rainfall rate field at 2245 UTC on 14 September 2015 with basin boundary for East Fork Virgin River and storm tracks of the Hildale storm from 2232 UTC to 2306 UTC. Outlet of the basin is denoted by a red star.

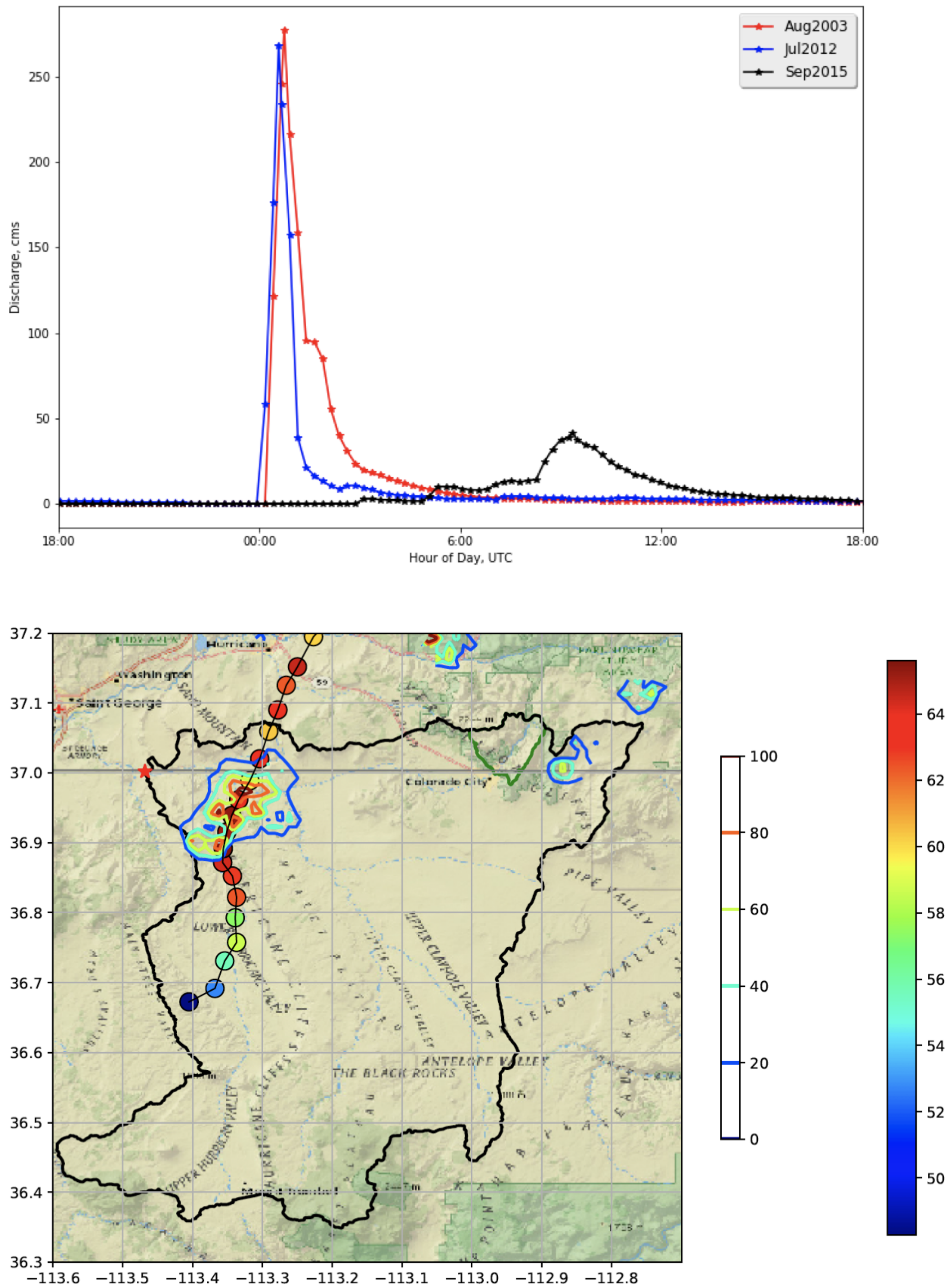

Figure 19. Discharge hydrographs (top) for Fort Pearce Wash on 15 August 2003 (red), 16-17 July 2012 (blue) and 14-15 September 2015 (black). Rainfall rate field at 2245 UTC on 16 July 2012 (bottom), with the Fort Pearce Wash basin boundary outlined in black; the outlet is denoted by a red star. The Short Creek boundary is outlined in green.

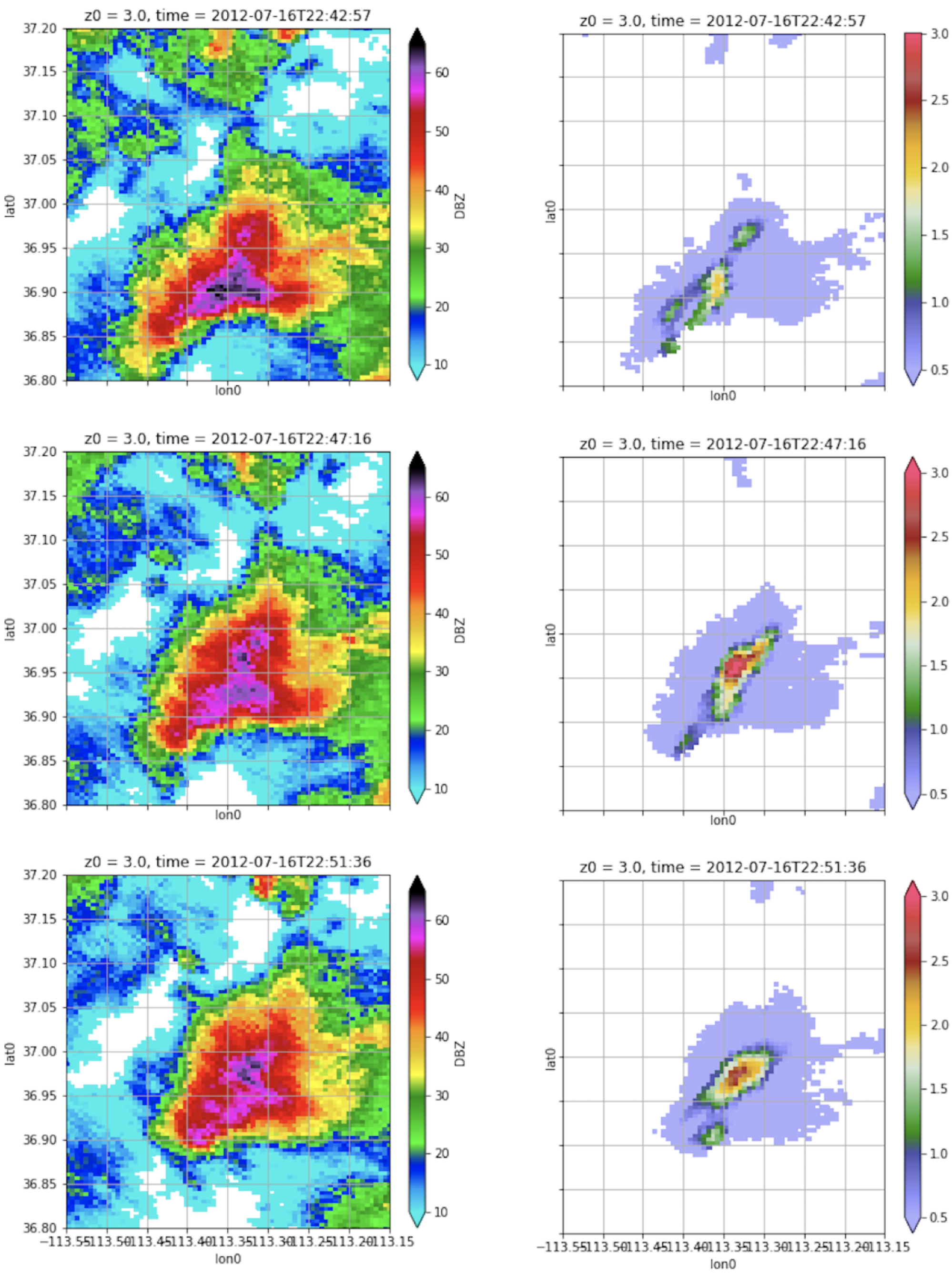

Figure 20. Reflectivity (left) and KDP (right) fields for for 2242 (top), 2247 (middle) and 2251 UTC (bottom) on 18 July 2012.

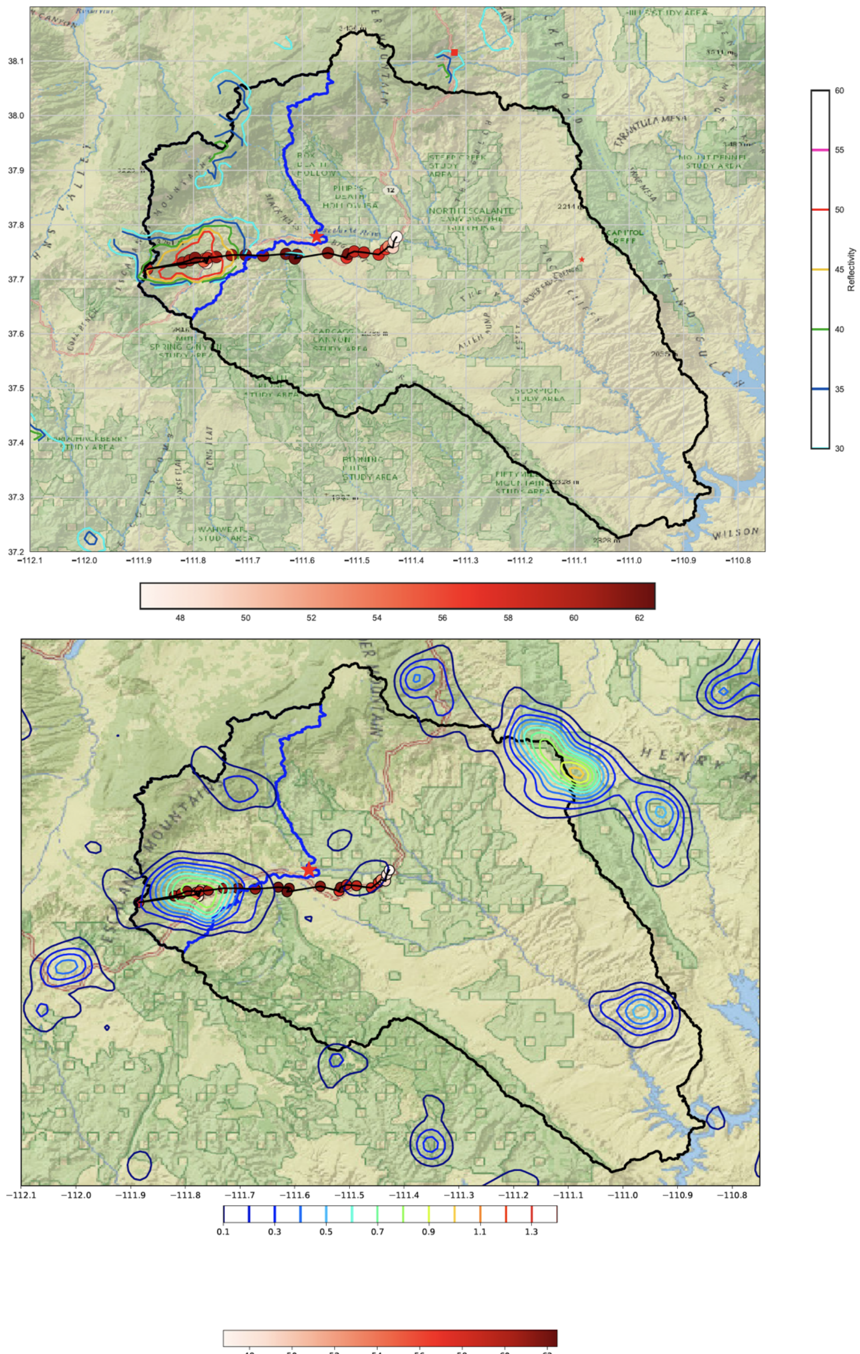

Figure 21. Reflectivity field at 1902 UTC for the 24 August 1998 storm that produced record flood peak in the upper Escalante River (top); storm tracks (1847 to 1957 UTC; moving west to east) are shown. Storm total lightning flash density is shown, with storm tracks, in the bottom panel. The USGS stream gage location is denoted by a red star.

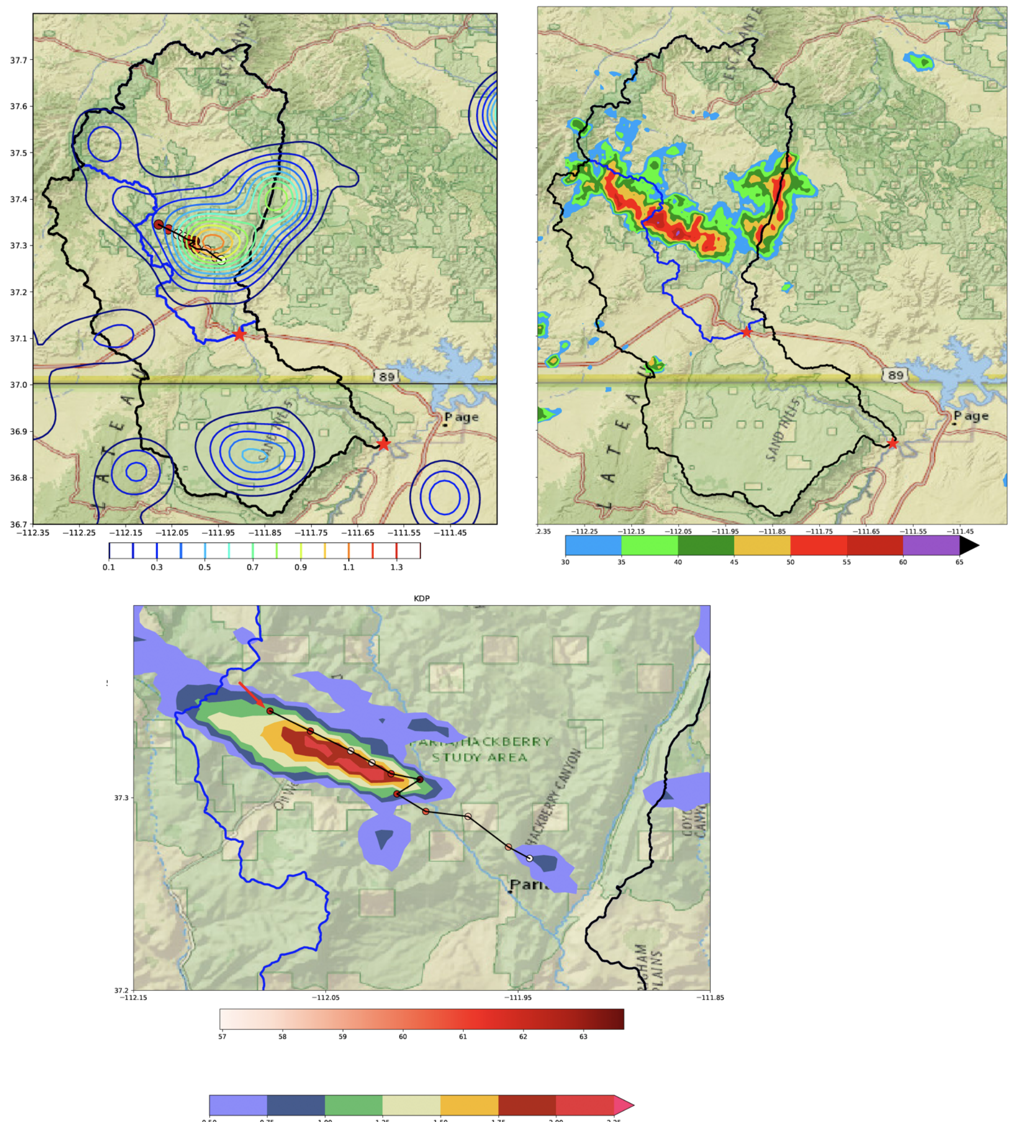

Figure 22. Storm total lightning flash density contours (CG strikes km^{-2}) with storm tracks for the 20-21 August 2012 Paria storm (upper left). Reflectivity field (dBZ) at 2046 UTC (upper right); closeup of K_{DP} field (degrees km^{-1}) at 2046 UTC with storm tracks (bottom). The red arrow in the bottom figure shows the location of the first tracked storm element. Stream gaging locations (red stars) and basin boundaries for the upper and lower Paria River are shown in the upper plots.

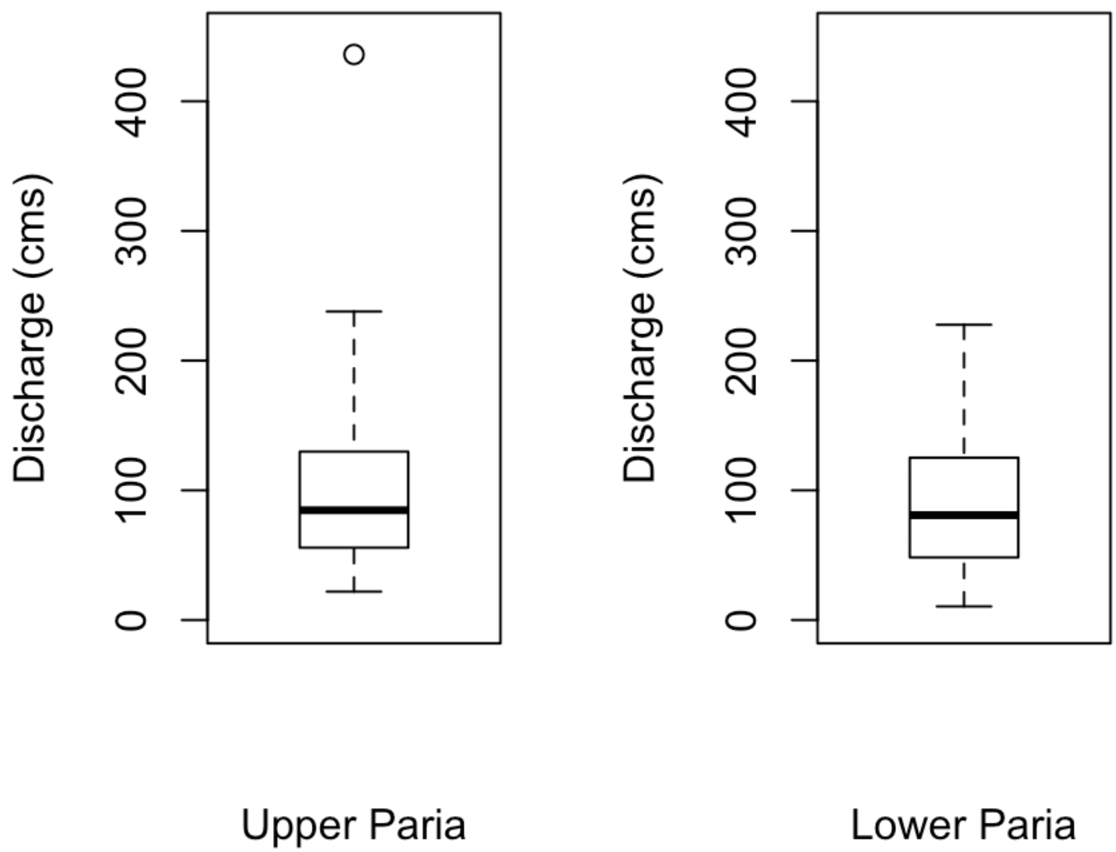

Figure 23. Boxplots of annual peak discharge for the upper Paria (left) and lower Paria (right) during the period of overlapping record.

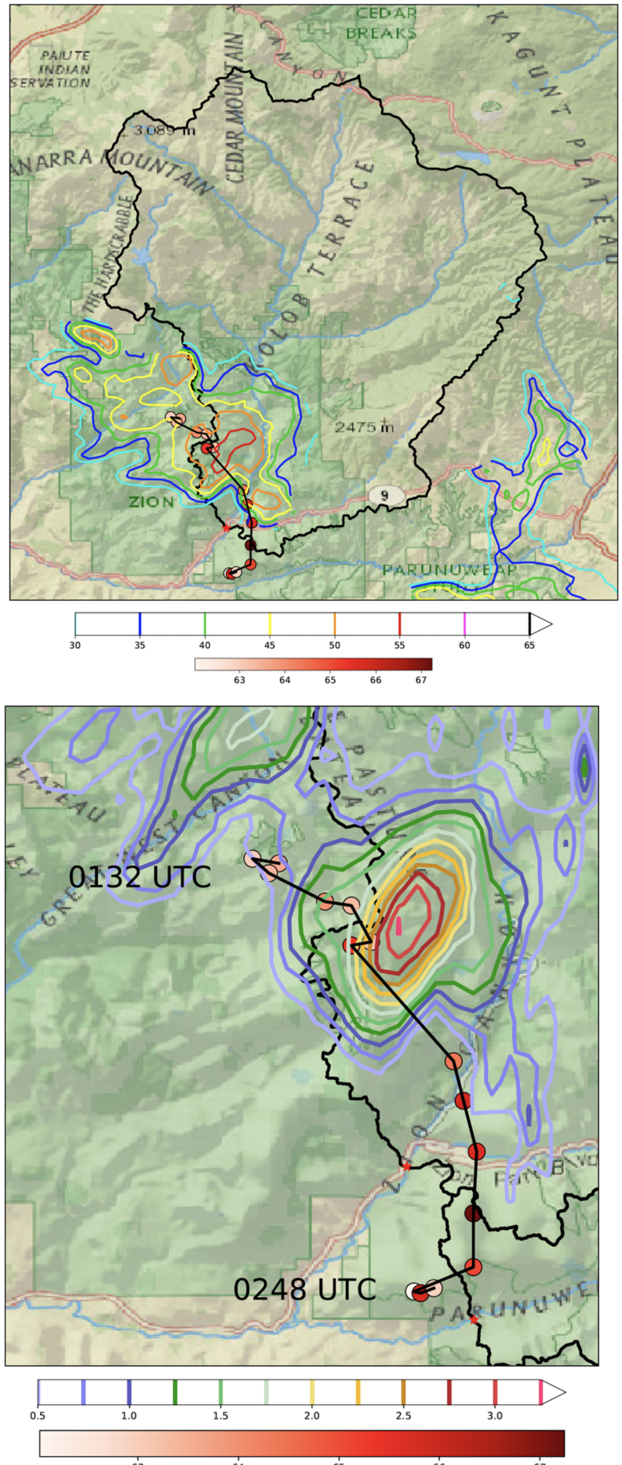

Figure 24. DPR rainfall rate contours (mm h^{-1}) at 0200 UTC on 12 July 2018 with storm tracks (top) and closeup with K_{DP} contours (degrees km^{-1}) and tracks (bottom).

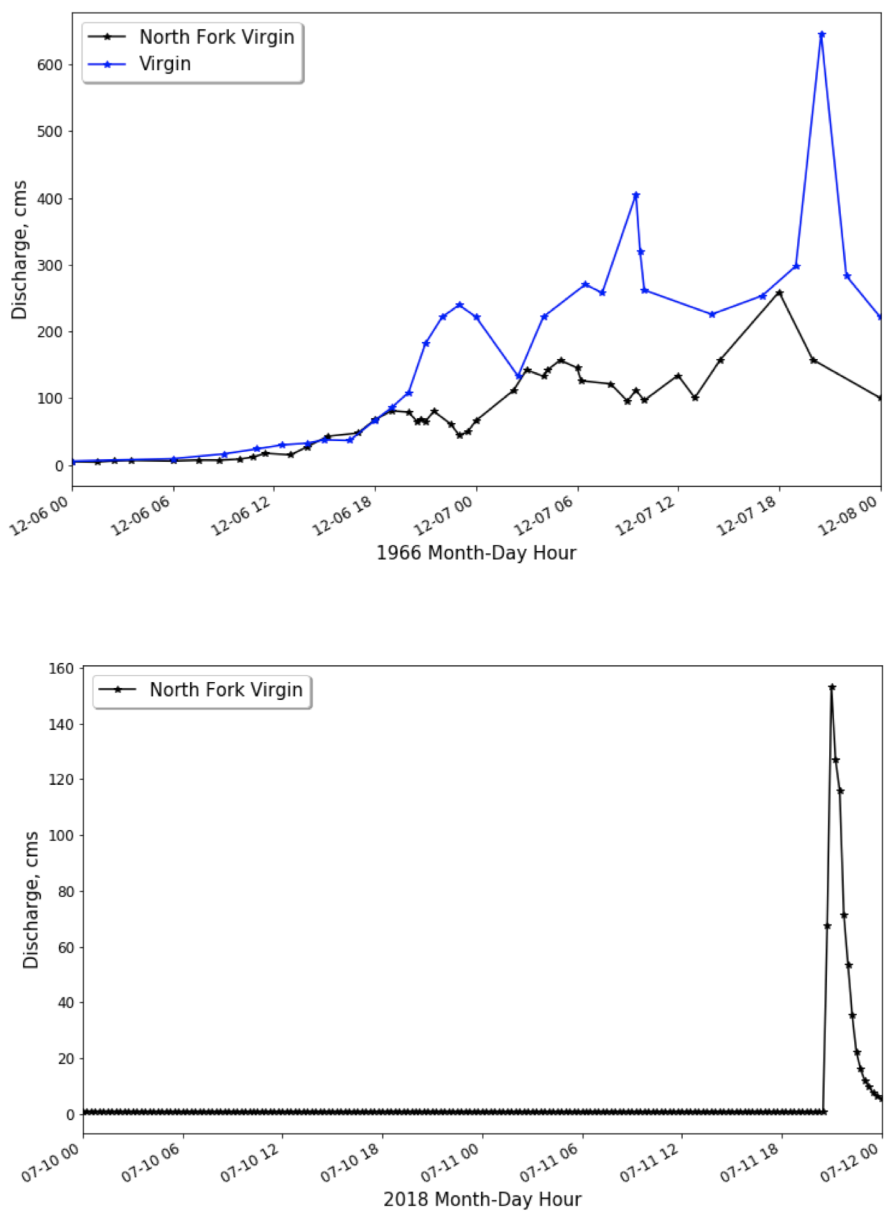

Figure 25. Discharge hydrographs for North Fork Virgin River (black) and Virgin River (blue) from 6 - 7 December 1966 (top); discharge hydrograph for North Fork Virgin River from 10 - 11 July 2018 (bottom).

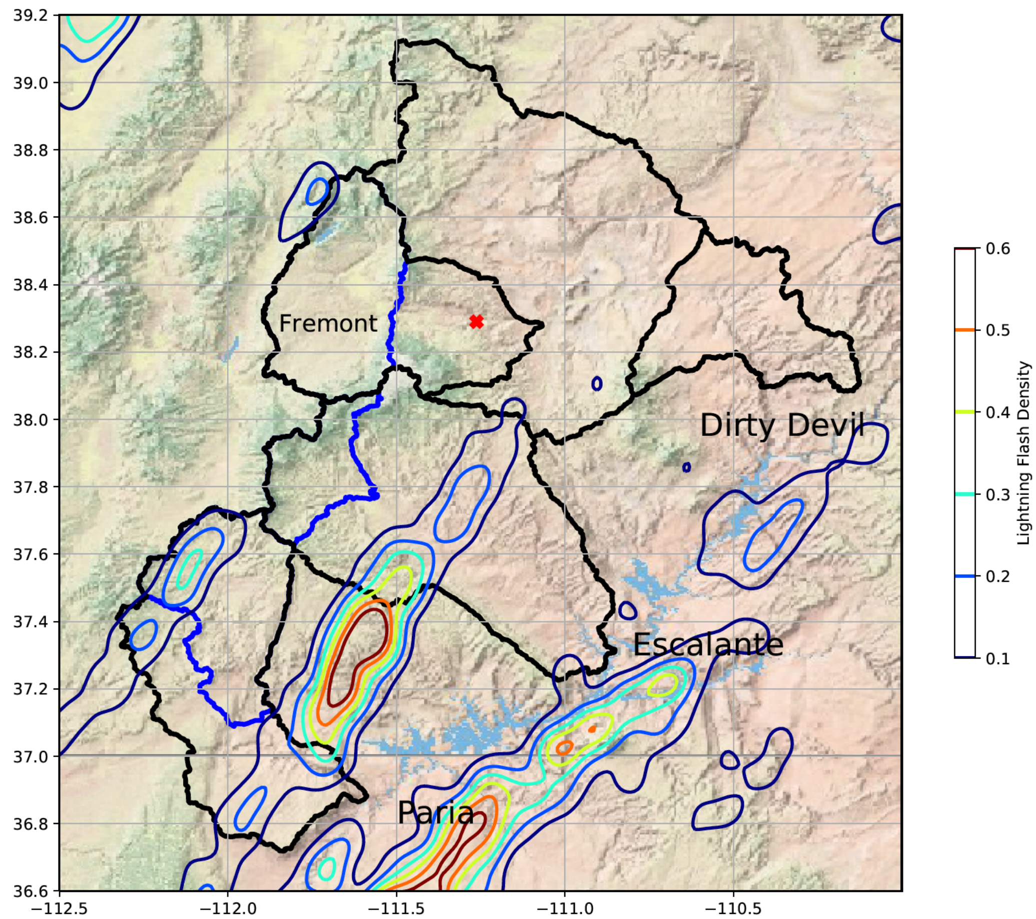

Figure 26. Storm total lightning flash density (CG strikes km^{-2}) from 1200 UTC, 5 October 2006 to 1200 UTC, 7 October 2006. Basin boundaries are outlined in black.

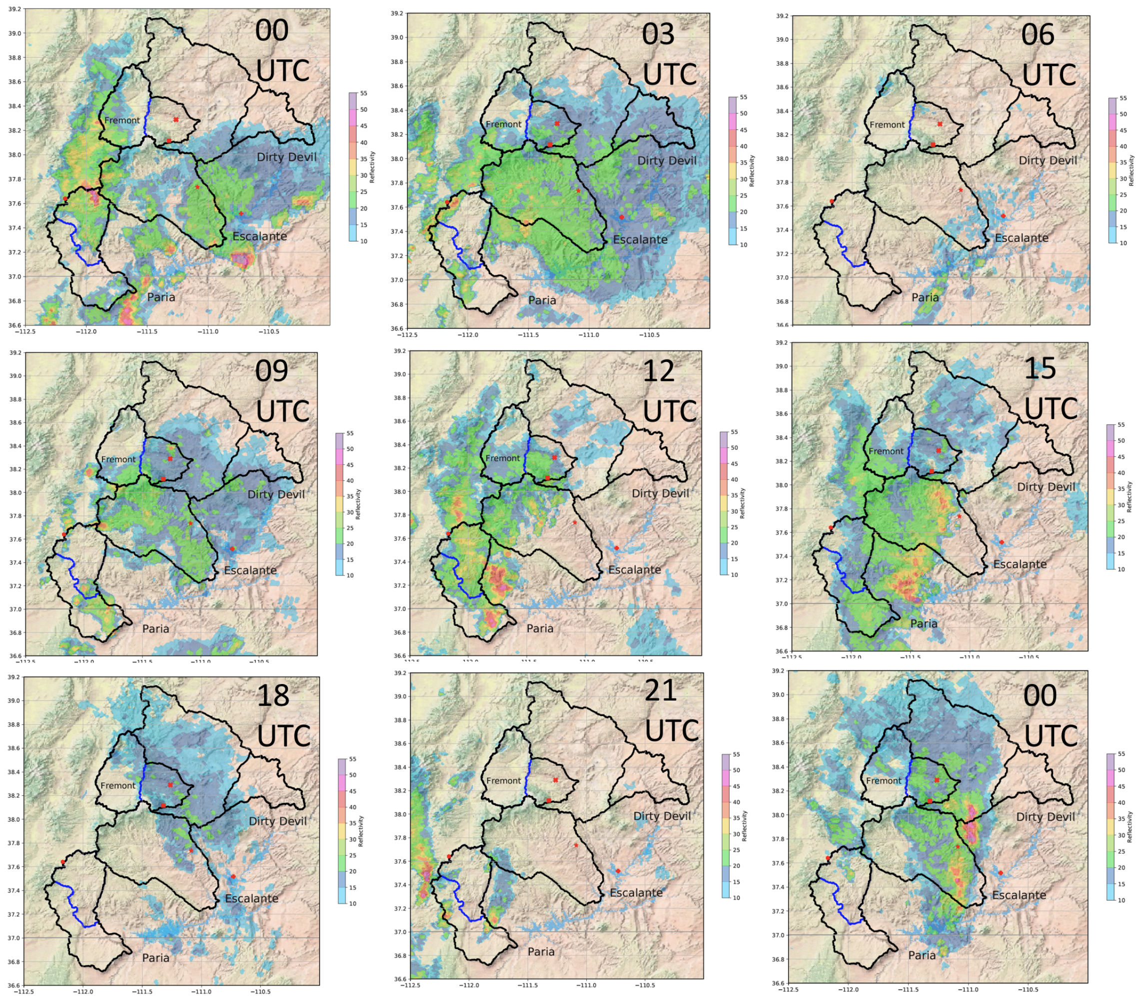

Figure 27. Reflectivity fields (dBZ) from 0000 UTC on 6 October 2006 to 0000 UTC on 7 October 2006 from the Cedar City WSR-88D. Basin boundaries are as in Figure 26.

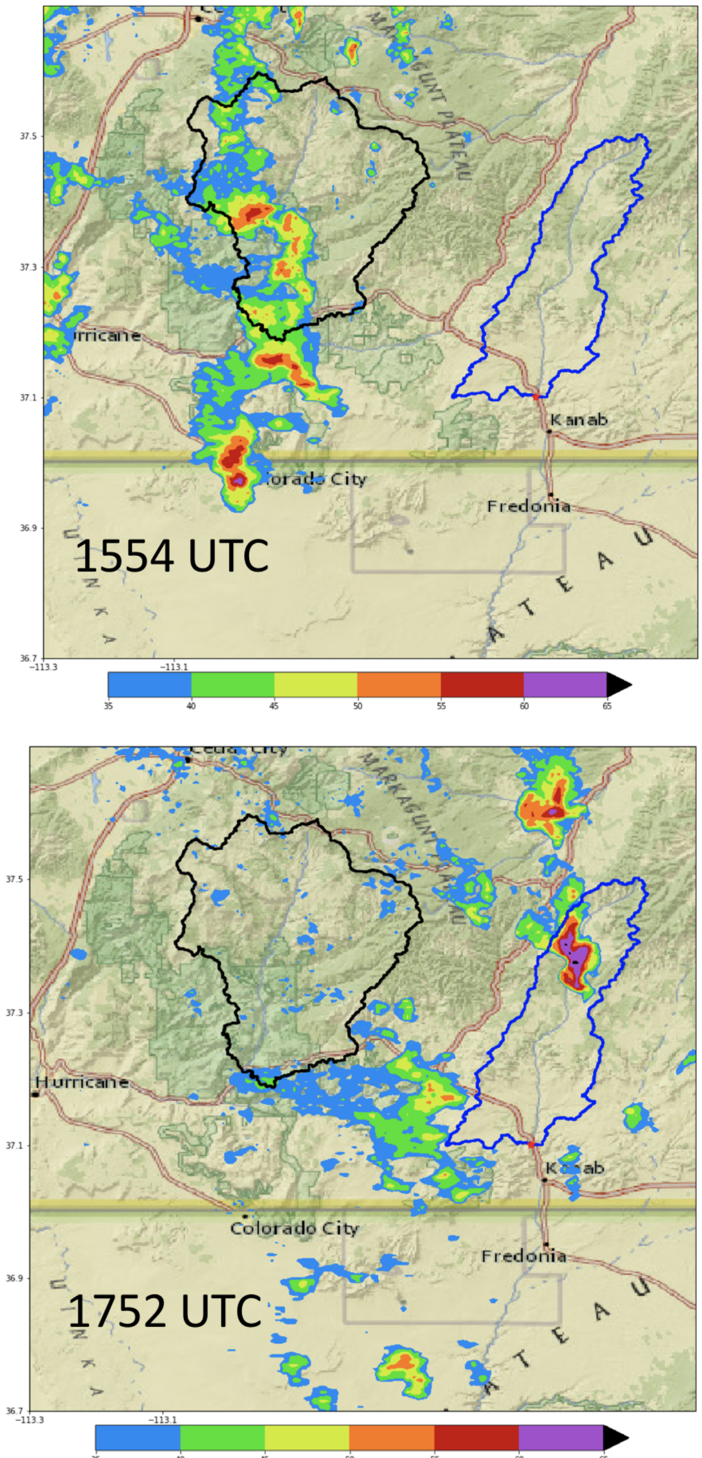

Figure 28. Reflectivity fields (dBZ) at 1554 UTC (top) and 1752 UTC (bottom) on 27 September 2014. Basin boundaries for the North Fork Virgin River (black) and Kanab Creek (blue) are shown.